GOETHE UNIVERSITÄT
FRANKFURT AM MAIN

A thesis submitted in fulfillment of the requirements for the degree of
Master of Science (M.Sc.) in Physical Geography

Hydrologic validation of a Structure-from-Motion DEM derived from low-altitude UAV imagery

Johann Wolfgang Goethe-Universität,
Frankfurt am Main

Author:
Florian Steiner
born January 20, 1988 in Ulm

Supervisors:
Dr. I. Marzolff
Prof. Dr. J. Wunderlich

November 30, 2015

Zusammenfassung

Aufgrund von Techniken wie *Structure-from-Motion* – einer Weiterentwicklung der Photogrammetrie – wird es zunehmend einfacher, hochauflösende Geländemodelle kostengünstig zu erstellen. Anders als in der konventionellen Photogrammetrie, bei der die Positionen, Ausrichtungen und Verzerrungen der Kameras bekannt sein müssen, sind diese beim SfM-Ansatz zu berechnen. Das Ziel dieser Arbeit ist es, diese DGMs auf der Grundlage von abgeleiteten, hydrologischen Parametern (Gerinnenetze und Einzugsgebiete) zu validieren. Als Referenz wurde ein konventionelles DGM, welches mit Hilfe der *Leica Photogrammetry Suite* erstellt wurde, verwendet. Um die Qualität verschiedener SfM-DGMs zu vergleichen, wurden vier Variationen mit unterschiedlichen Bildern als Grundlage in zwei unterschiedlichen räumlichen Auflösungen erstellt (ca. 4,5 und 10 cm). Es wird ein Überblick über die Methoden zur Erstellung der DGMs in *Agisoft PhotoScan* gegeben. Außerdem werden die Schritte zur Erstellung und zum Vergleich der hydrologischen Daten in *ESRI ArcGIS* beschrieben. Die Ergebnisse zeigen, dass SfM die visuelle Qualität der DGMs enorm steigert. Die Fehler der Bodenpasspunkte sind kleiner und weisen nicht den gleichen systematischen Kuppel-Effekt wie das LPS-DGM auf. Die Hauptcharakteristika der abgeleiteten Gerinnenetze sind gleich, obwohl Unterschiede messbar sind: 32–38 % der SfM-Gerinnenetze unterscheiden sich vom LPS-Netzwerk. Die Ergebnisse der untersuchten Einzugsgebiete kennzeichnen sich dadurch, dass kleine Unterschiede in den Gerinnenetzen große Unterschiede in den Einzugsgebieten verursachen können (bis zu 29 %).

Structure-from-Motion bietet aufgrund der einfachen Anwendbarkeit und dem hohen Grad der Automation neue Möglichkeiten im Bereich der Geowissenschaften. Obwohl die Ergebnisse vielversprechend sind, kann die Anwendbarkeit der SfM-DGMs auf hydrologische Fragestellungen aufgrund der verwendeten Referenzdaten und der verwendeten Stichprobengröße nicht abschließend bestätigt werden. Weitere Untersuchungen sind notwendig, um systematische Probleme zu beseitigen (Kuppel-Effekt) und die angewandten Methoden zu verbessern (Vergleich von Gerinnenetzen und Einzugsgebieten).

Abstract

Using new techniques like *Structure-from-motion* (SfM) – an innovative evolution of photogrammetry – it is becoming increasingly easy to generate high-resolution DEMs at low costs. The approach is – unlike in conventional photogrammetry – based on the calculation of camera locations, orientations and distortions without the previous knowledge of any measurements. This work aims at validating these DEMs using derived hydrologic data (drainage networks and watersheds). As a reference a DEM that was created using the *Leica Photogrammetry Suite* was used. To compare the quality of different SfM-DEMs, four variations using different images as input and different spatial resolutions were calculated (between 4.5 and 10 cm). An outline of the methods used to create the DEMs using *Agisoft PhotoScan*, as well as a description of the steps performed to generate and compare the hydrologic data in *ESRI ArcGIS*, is given. The results reveal that SfM highly increases the visual quality of the DEMs. GCP errors are smaller and do not show the same systematic doming effect visible in the LPS-DEM. The main characteristics of the derived drainage networks are the same for both methods, although differences are measurable: 32–38 % of the SfM-networks are different compared to the LPS-network. The results of the analyzed watersheds reveal, that small differences in the drainage networks may cause large differences in the watersheds (up to 29 % differences).

Structure-from-Motion offers new possibilities for geosciences due to the easy application and the high degree of automation. Although the results are promising, the applicability of SfM-DEMs for hydrologic questions cannot be finally confirmed due to the reference data used and the small sample size. Further studies are necessary to eliminate systematic problems (doming effect) and to improve the applied methods (comparison of drainage networks and watersheds).

Erklärung

Ich versichere hiermit, dass ich die vorliegende Arbeit selbstständig verfasst und keine anderen als die im Literaturverzeichnis angegebenen Quellen benutzt habe. Alle Stellen, die wörtlich oder sinngemäß aus veröffentlichten oder noch nicht veröffentlichten Quellen entnommen sind, sind als solche kenntlich gemacht. Die Zeichnungen oder Abbildungen in dieser Arbeit sind von mir selbst erstellt worden oder mit einem entsprechenden Quellennachweis versehen. Diese Arbeit ist in gleicher oder ähnlicher Form noch bei keiner anderen Stelle zur Prüfung eingereicht worden.

Mainz, den 30. November 2015

Florian Steiner

Contents

List of Figures

List of Tables

Nomenclature

DEM	Digital Elevation Model
DGPS	Differential Global Positioning System
DN	Drainage Network
DSM	Digital Surface Model
GCP	Ground Control Point
GSD	Ground Sample Distance
IMU	Intertial Measurement Unit
LiDAR	Light Detection and Ranging
LPS	Leica Photogrammetry Suite
MVS	Multi-View Stereo
RMSE	Root Mean Squared Error
SFAP	Small-format Aerial Photography
SfM	Structure-from-Motion
SIFT	Scale Invariant Feature Transform
SRTM	Shuttle Radar Topography Mission
TLS	Terrestrial Laser Scanning
UAV	Unmanned Aerial Vehicle

1. Introduction

Digital Elevation Model (DEM) is a term for the digital and numerical representation of earth's surface. High-resolution DEMs are an important source of information for geoscientific applications in science and industry (Wechsler 2007: 1482). They allow for analyses and especially quantifications in surface morphology (soil-erosion, landslides, gully-erosion, river- and coastal morphology), hydrology (drainage networks), tectonics and volcanism, glaciers, oceanography and even space research (Pike et al. 2009: 25 f.; Tarolli 2014: 296 f.; Tarolli and Dalla Fontana 2009).

The generation of these DEMs has changed over the time. While the first DEMs were calculated semi-automatically from contour lines, they are nowadays generated using remote sensing data. These are mainly satellite imagery (e.g. SRTM, ASTER, ALOS), airborne and terrestrial LiDAR and photogrammetry. Regarding the scales, *Small-format Aerial Photography* (SFAP) closes a gap between field studies and satellite imagery (D'Oleire-Oltmanns et al. 2012: 3392).

All methods have advantages and disadvantages: Remote sensing from space allows for a great coverage, which is why most DEMs of this category are almost globally available. However, they are expensive to produce and currently have a spatial resolution of only up to 5 m. Terrestrial or airborne LiDAR is capable of producing higher resolutions (up to millimeters) and can be used to filter vegetation cover, but it is still time and money-consuming. Photogrammetry in general can produce high-resolution DEMs at lower costs, yet high expertise, knowledge and thorough preparation is needed.

Structure-from-Motion (SfM) is an approach for generating DEMs using photogrammetric principles without the initial knowledge of interior and exterior parameters (see Section 2.2). *Structure* refers to the 3D-coordinates and *Motion* to the positions of the cameras, meaning that the structure is retrieved from the motion of the camera (Grossmann and Santos-Victor 2000: 685). Within the last few years, software-applications have been developed that make it extremely easy to generate DEMs using the SfM-technique (Agisoft PhotoScan, VisualSFM, Pix4Dmapper, 3DFlow Zephyr). Additionally, UAVs for taking aerial images are getting increasingly inexpensive and easy to use. It is already possible to purchase a drone that automatically covers a specific area at the click of a button and takes the necessary images, for less than 1,000 €. In a further step, the images are automatically processed and exported to a DEM. This example illustrates that there are easy and affordable tools to create high-resolution DEMs. However, the validation of such high-resolution DEMs is an important step, since "high resolution" not necessarily means "high precision". Although the results may be visually promising, they need to be validated and thoroughly tested before this will become the method of choice for geoscientific applications (Fonstad et al. 2013: 427).

1.1. Previous Research

Some research has been conducted to verify the accuracy of SfM-DEMs. Many studies use LiDAR-data (Fonstad et al. 2013; James and Robson 2012; Westoby et al. 2012) and GPS (Tonkin et al. 2014) as a reference to determine the accuracy of the SfM-approach. Although LiDAR itself is a relatively new technique, it is the best available reference. One advantage is that data for all points of the point cloud is collected (Vaze et al. 2010: 1088). In contrast, GCPs allow for high accuracies – using differential GPS or total station surveys – while being a well known technique.

Fonstad et al. (2013) performed a validation of SfM-data using LiDAR and GCPs. The authors directly compared the point clouds without at first interpolating a raster of the elevation surface (DEM). According to their study, the mean distance to GPS-points was 0.21 m for the SfM-model and 0.44 m for the LiDAR-model (Fonstad et al. 2013: 425). They conclude that for images taken from low altitudes (in their study approx. 40 m) the accuracies of DEMs derived from using SfM are comparable to LiDAR or even better, when surveying bare soil. The authors state that the SfM-approach provides benefits for many applications due to highly reduced costs. Yet it needs further investigation (Fonstad et al. 2013: 427).

In another study, Lucieer et al. (2014) mapped landslide displacements using SfM and validated these using 39 independent DGPS points. They took 238 images from an UAV with a spatial resolution of 1 cm and processed these in *Agisoft PhotoScan*. The RMSE for vertical accuracy using the 39 independent DGPS points was 6.2 cm. Their results indicate that the use of UAV-imagery and SfM-algorithms is suitable for monitoring landslides.

Westoby et al. (2012) analyzed the performance of SfM compared to TLS in three different sites: a coastal cliff, a breached moraine-dam complex and a bedrock-ridge. They used the popular bundle adjustment system *Bundler* (Snavely et al. 2008) and *Multi-view Stereo* algorithms (CMVS, PMVS2) to calculate dense point clouds. Their results for the coastal cliff reveal that 86 % of the differences between SfM and TLS are in a range between -1.0 and 1.0 m at a ground resolution of 1 m. The total GCP-error for the other sites was 0.226 m (moraine-dam of 650 m length, resolution: 1 m) and 0.003 m (bedrock of 80 m length, resolution: 0.1 m). According to the authors, SfM offers new possibilities and advantages for geoscientific applications due to low costs, simple applicability and a high degree of automation, especially in remote and inaccessible regions (Westoby et al. 2012: 313).

1.2. Aims of This Work

This work has several important objectives. Besides the need for further analysis of the overall accuracy of SfM-DEMs, the question whether these models are suitable for hydrologic applications remains unanswered. The general aim of this work is the validation of a SfM-DEM using derived hydrologic data. The main objective of this work is therefore to generate a DEM using SfM-algorithms, to derive common hydrologic parameters and data and to validate these parameters using a DEM created using more conventional photogrammetry. SfM-DEMs could already be assessed equally well or even better than LiDAR-data (Fonstad et al. 2013: 422). This encourages the assumption that, compared to other high-resolution DEMs, SfM-DEMs are equally suitable for hydrologic ap-

plications, such as the generation of drainage networks or the delineation of watersheds.

It is assumed that statistical values describing the accuracy of DEMs may not reflect the accuracy of DEMs regarding hydrologic applications. DEMs created using the SfM-approach can be statistically comparable or better than other DEMs, however, still cause the derived hydrologic data to be faulty, due to systematic errors in the process. In order to validate the SfM-approach itself, several SfM-DEMs will be generated using different sets of images. The hypothesis is that the use of more diverse images results in DEMs that are better in terms of the accuracy and better in representing hydrologic features. This is based on the work of several authors who previously analyzed the accuracy of SfM-DEMs (James and Robson 2014; Wackrow and Chandler 2008, 2011). They stated that more and convergent images improve the quality of derived point clouds or DEMs.

Regarding the hydrologic approach, it has to be noted that it is not the aim of this study to accurately identify gullies. This approach aims at comparing common hydrologic parameters derived from DEMs created by using different methods (conventional photogrammetry and SfM). The general statement does not aim at how accurately the different models represent reality, but rather how similar the results from different methods are. Since no other reference dataset (e.g. LiDAR) is available, the conventional photogrammetric approach using the *Leica Photogrammetry Suite* will be used as a reference.

2. Background and Theory

The meaning of *high-resolution* related to DEMs has changed over the years. The first, nationwide available DEMs had a spatial resolution of 63 m and were calculated semi-automatically from contour lines (Pike et al. 2009: 20). Today's most commonly used elevation data come from the NASA Shuttle Radar Topography Mission (SRTM), which was flown in 2000. It resulted in an almost globally available[1] dataset of elevation data with a spatial resolution of one arc-second – which is equivalent to around 30 m at the equator (Lillesand et al. 2008: 705). Tarolli and Dalla Fontana (2009: 1) described this data set as a "high resolution [...] database".

Widely available datasets at higher resolutions are planned for the upcoming years. For example *ALOS World 3D* at a spatial resolution of 5 m and *TanDEM-X* with up to 1 m (Bartusch et al. 2009). Nevertheless, these datasets are not yet available and will be associated with (very) high costs.

Other techniques like *Structure-from-Motion* or LiDAR may be an alternative for small to medium sized areas of investigation. They can provide higher resolutions of up to a few centimeters or even millimeters. Nouwakpo et al. (2014) for example analyzed the performance of SfM compared to the conventional photogrammetric approach using *Leica Photogrammetry Suite* (LPS) in microtopographic applications. Their resulting DEM had a spatial resolution of 1 mm calculated from an average point density of 35.9 points/cm² (Nouwakpo et al. 2014: 312).

Small-format Aerial Photography is one possibility for creating high-resolution DEMs. It is based on consumer-grade film- or digital-cameras that lack the geometric accuracy and calibration of professional mapping cameras. However, they are available at lower costs in a range of several 1,000 € (Aber et al. 2010: 11). These cameras are carried by manned (helicopters, hot air balloons) or unmanned platforms (fixed-wing model planes, small multicopters, kites, blimps, balloons) and provide images from heights between only a few meters and up to several hundred meters.

The following Chapter 2 gives an introduction to the basics of today's most commonly used method of photogrammetry – hereafter referred to as "conventional photogrammetry" (Section 2.1) – and the new approach that has been developed during the last decade: *Structure-from-Motion* (Section 2.2). Another commonly used method is LiDAR, which uses laser-beams to determine distances between several reference points and often millions of measurement points. It is often used as a reference for the validation of the SfM-approach.

2.1. Conventional Photogrammetry

Lillesand et al. (2008: 123) describe photogrammetry as "the science and technology of obtaining

[1] Since 7th of August 2015, the high resolution of 1 arc-second is globally available. Until then, the areas outside the US were available at a resolution of only 3 arc-seconds (NASA 2015).

spatial measurements and other geometrically reliable derived products from photographs". The concept of photogrammetry has been known for more than 150 years and has been developed from an analog procedure using films and specialized machines to manually process these (e.g. a stereocomparator for measuring image coordinates on stereopairs, see LILLESAND ET AL. 2008: 131) to a digital discipline using consumer-grade digital cameras and computers (ABER ET AL. 2010: 23). Photogrammetry can be used to produce DEMs, orthophotos and thematic GIS data. Measurements of height, length, area and volume are possible.

The conventional photogrammetric approach relies on known positions and specifications (external and internal parameters) of 2-dimensional images taken from different positions in order to reconstruct 3-dimensional objects. The basic principle is the reconstruction of paths of rays between the image plane and the object using triangulation. Fundamental for this is the knowledge of the camera scale ($S = d/H = f/H_g$) in order to calculate and measure actual surface dimensions.

As Figure 2.1 illustrates, the exterior orientation is determined by the position of the camera (X, Y, Z) and the rotation (ω, ϕ, κ). Internal parameters are the focal length (f), several coefficients of radial lens distortion and principal point coordinates (o) (ABER ET AL. 2010: 26). The in- and external parameters need to be known at the highest possible accuracy, as small errors are multiplied and can cause huge errors in the calculated data.

In large-format aerial photogrammetry, the external orientation may be measured by using the accurate combination of GPS and *Inertial Measurement Unit* (IMU). The external orientation may also be determined by *Ground Control Points* (GCP) that need to be marked in the field and measured with high accuracies of centimeters or below. These accuracies are commonly reached using a total station survey (ABER ET AL. 2010: 27). To avoid the need for at least three GCPs per image, the so-called bundle-block adjustment can be performed, combining several images in blocks. The images in one block are connected using image points (tie points) that appear in two or more images (ABER ET AL. 2010: 32). The term *bundle* refers to the bundle of light rays that are adjusted in order to ideally fit the object and camera position. This means the internal and external parameters are adjusted "in one bundle" (TRIGGS ET AL. 1999: 298 f.).

Using the external and internal orientation, image pairs showing the same features (A) from different positions and angles can be established. Reconstructing the ray paths ($\overline{a_1 A}$ and $\overline{a_2 A}$, respectively) for the same feature in two images results in an intersection of the lines – assuming the internal and external orientations were accurately measured. In the idealized Figure 2.1, the intersection (A) represents the original position of the feature on the surface and their coordinates in space can be calculated. In reality, their will always be a small difference between the intersection and the original object feature. The difference between these is called the *reprojection error*.

2.2. The Principle of Structure from Motion

Especially in UAV-based remote sensing, the measurement of accurate internal and external parameters is often associated with high costs. Small aircrafts, kites or balloons might not be able to carry the weight of such measuring systems. Structure-from-Motion eliminates the need for these measurements, since the parameters are calculated directly from the highly redundant images, by means

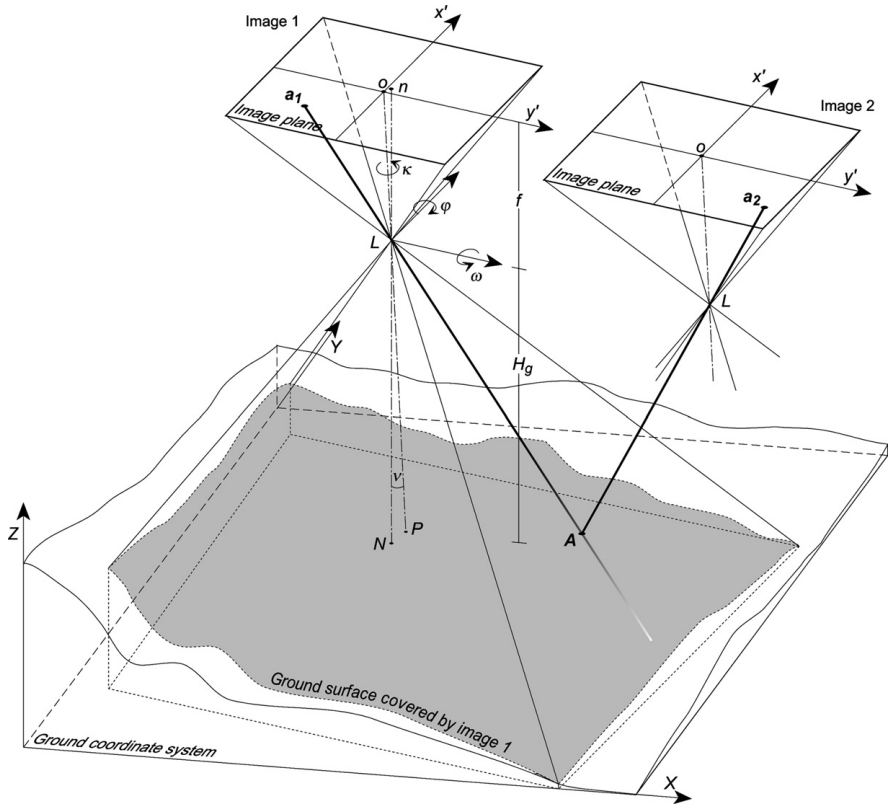

Figure 2.1.: Schematic illustration of reconstructing ground coordinates using space-forward intersection (Aber et al. 2010: 31)

of a bundle adjustment. This technique was developed in the 1990s (Westoby et al. 2012: 301) and is based on the same mathematical principles as the conventional photogrammetry.

At first, distinct feature points are detected in all images and matched using for example the *Scale Invariant Feature Transform* (SIFT) keypoint detector algorithm, which provides the location of each point and a local descriptor. The local descriptor needs to be distinctive and invariant to different conditions like viewing angles, images resolutions and illuminations (Lowe 2004: 100). This algorithm is one of the main differences to conventional photogrammetry, because it allows for unstructured image acquisition, unlike in conventional photogrammetric applications, where parallel flight plans are used to acquire near-orthogonal, overlapping images (Fonstad et al. 2013: 422). *Agisoft PhotoScan* – the SfM-software used in this study – does not use the SIFT algorithm, but apparently[2] a similar algorithm with a "little bit higher alignment quality". The camera parameters are then reconstructed and optimized by minimizing the reprojection error, which is the sum of distances between the projections and the corresponding image features. The SfM-approach uses a bundle adjustment to iteratively refine the model during image alignment (Snavely et al. 2008: 7).

Another difference to the conventional photogrammetric approach is that SfM first estimates relative camera locations and the GCPs are introduced afterwards. However, some newer SfM-applications use GCPs in the beginning to estimate initial camera positions. Additionally, some approaches for conventional photogrammetry solve the equations before the GCPs are identified. Thus, according to different authors (Fonstad et al. 2013: 422; James and Robson 2014: 1415), the two approaches are not developing divergently.

Finally, a dense point cloud is calculated based on the sparse point cloud and the calculated camera positions (Westoby et al. 2012: 303). This can be accomplished by using a *Multi-View Stereo* (MVS) algorithm like PMVS2 (see Furukawa and Ponce 2007).

Structure-from-Motion offers advantages over conventional photogrammetry: the possibility to use small, uncalibrated cameras (although there are some limitations concerning possible accuracies), the possibility to take unstructured images and the high degree of automation (Westoby et al. 2012: 303).

2.3. Common Problems in Photogrammetric Applications

One of the most commonly observed problems using SfM is the so-called doming effect (see James and Robson 2014: 1416; Wackrow and Chandler 2011: 21; Wackrow and Chandler 2008: 8). It is characterized by a systematic distortion of the DEM resulting in an overall dome or bowl (see Figure 2.2). It is often proposed to take pictures from different, converging angles to minimize the error (James and Robson 2014: 1417). Wackrow and Chandler (2008) conducted a simulation to analyze the influence of a convergent image configuration on the systematic error. They created a virtual DEM and calculated perfect photo-coordinates using predefined in- and exterior parameters for the virtual camera. These photo-coordinates were then recalculated to the object-coordinates using a bundle adjustment. For their testfield of 1.4×1.3 m, they calculated a mean error of -0.9 mm

[2] Presumably due to the commercial concept, the algorithms used in *Agisoft PhotoScan* are not well documented. This statement was made by a member of the Agisoft technical support.

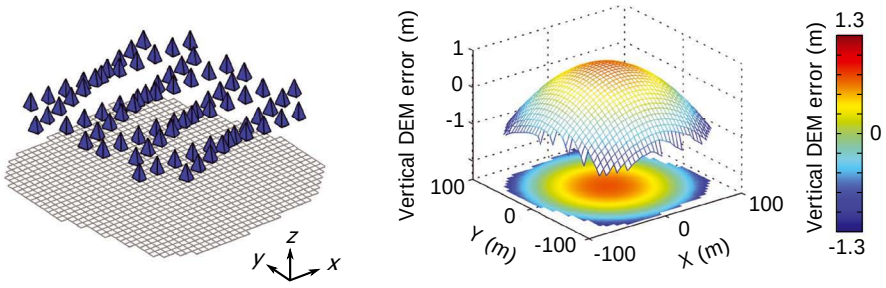

Figure 2.2.: Vertical DEM error in practical SfM-simulation processed with self-calibration of radial distortion (after James and Robson 2014: 1417, adapted)

for the normal case and -0.1 mm for the convergent case, improving the accuracy by a magnitude of 6 (Wackrow and Chandler 2008: 13). This effect was also analyzed by James and Robson (2014), who attribute the cause to the combination of a near-parallel direction of image acquisition and inaccurately calibrated lens distortion. Since every camera – especially every consumer camera – has some kind of a distortion, it is recommended to calibrate the camera prior to taking the pictures. This calibration might improve the overall accuracy (James and Robson 2014: 1419) since there is no need for the bundle alignment procedure to calculate the camera model. However, accurate camera calibrations are not readily available for those consumer-grade cameras often used in SfM-applications. Furthermore, the same effect may occur using a camera self-calibration procedure in conventional photogrammetry.

Another problem for any photogrammetric approach creating DEMs is vegetation (Aber et al. 2010: 38). The DEM refers to the bare soil, which is often covered by vegetation, hiding it from the view of the camera. These areas are therefore not visible in images and thus cannot be reconstructed. The LiDAR-technique has the advantage that laser beams may penetrate the vegetation cover and return a signal from the ground. Resulting point clouds can then be filtered to only represent the ground surface (DeLong et al. 2012: 264). Several studies have attributed vegetation cover with higher errors in SfM-models, compared to bare soil (Westoby et al. 2012: 307; Mancini et al. 2013: 6892; Tonkin et al. 2014: 40; Fonstad et al. 2013: 426).

3. Data and Methods

This chapter defines the study area (Section 3.1) and lists all data and methods used in this thesis. The images and GCPs used in this analysis were taken in 2011 and it was initially not planned to use them for this kind of analysis. It has to be made clear that the data was not collected by the author himself. Nevertheless, brief descriptions of the UAV (Section 3.2) and the data acquired are given (Section 3.3). For more details on the data acquisition, the reader is referred to D'Oleire-Oltmanns et al. (2012). Section 3.4 describes the software and methods used to process and analyze the images used in this work. The two main parts of the analysis are the generation of DEMs using *Agisoft PhotoScan* and the hydrologic analysis of these DEMs using *ESRI ArcGIS*.

3.1. Study Area

The study area chosen is located near the city of *Taroudannt* in the semi-arid southern part of Morocco situated in the *Souss Valley*. The *Souss* basin drains into the *Souss* river and is framed by the High-Atlas Mountains in the north and the Anti-Atlas Mountains in the south. The depression of the basin is filled by Pliocene and Quaternary deposits covered by alluvial fans and terraces (Peter et al. 2014: 26; Bhiry and Occhietti 2004: 315). The area has a "negative water balance [...] due to the precipitation of only around 200 mm and a mean annual temperature of 20°C" (Peter et al. 2014: 26). The land use of the valley is characterized by large agricultural fields of citrus and banana plantations, which are more and more replaced by greenhouses covered in clear plastic foil. Due to the low amount of precipitation, the fields are irrigated by deep wells (Peter et al. 2014: 26). The general vegetation cover is characterized by "subtropic, desert and Mediterranean species" (Peter et al. 2014: 26).

The study area are badlands on the alluvial fan of *Oued Irguitène*, which originates from the High-Atlas Mountains. The area lies within 30°28'05" and 30°28'01" northern latitude and 8°56'36" and 8°56'48" western longitude. The total area of the field is around 5 ha, although the actual area of investigation is slightly smaller: 4.49 ha. The area was chosen to fit all elevation models created. It is characterized by aggressive rill and gully erosion and features different types of surfaces: flat and featureless areas and deeply incised heterogeneous areas. Since 2000, it was leveled with the help of bulldozers several times in order to use it as an agricultural field (Peter et al. 2014: 27). Soil parameters of the study area were analyzed by Peter et al. (2014). They measured a pH-value of 8.29, a proportion of 5.88 % of organic matter, a bulk density of 1.59 g/cm^3 and a mean grain diameter of 0.08 mm.

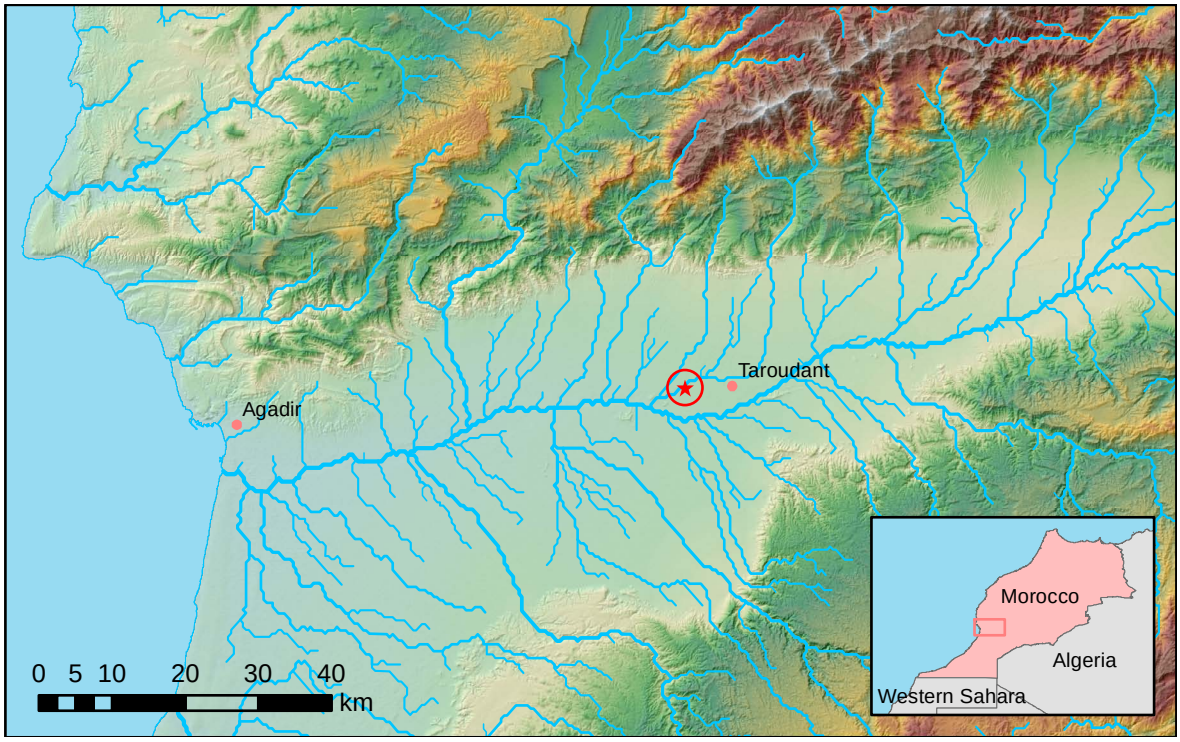

Figure 3.1.: The *Souss Valley* in Morocco and the location of the study area (elevation data: SRTM 1 Arc-Second Global, available from the *U.S. Geological Survey*; hydrographic information: Lehner et al. 2006; borders: GADM database, available at www.gadm.org)

3.2. UAV Specifications

The images were taken by D'Oleire-Oltmanns et al. (2012) on November 17, 2011, using a fixed-wing UAV (Sirius I by *MAVinci*, Germany). The system has a wingspan of 163 cm, a total length of 120 cm and a weight of 2.3 kg (without payload). According to D'Oleire-Oltmanns et al. (2012: 3395), "at a ground speed of 45–85 km/h, the flight time with 550 g payload and one battery is up to 40 min". There is no need for a pilot that controls the aircraft through the area of investigation, since it is equipped with the *MAVinci* autopilot. The area is defined prior to the flight and the waypoints are automatically calculated according to settings like GSD and overlap of images. Nevertheless, there is an assisted flying mode, which allows the pilot to easily control the UAV manually, while the autopilot with its GPS and IMU adjusts for any unforeseen influence (e.g. height loss) and restricts user actions to avoid damage (e.g. maximum values for pitch and roll) (D'Oleire-Oltmanns et al. 2012: 3396).

The UAV is equipped with a mirror-less digital camera with an interchangeable lens. The Panasonic Lumix DMC-GF1 – used in this campaign – is combined with a 20 mm single focal length pancake lens. This setup is much smaller and lighter than traditional SLR cameras. The micro four-thirds sensor has a resolution of 12.1 MP, a size of 17.3×13.0 mm and is capable of taking RAW-images. The resulting picture element size – the physical size of each pixel on the sensor – is approx. 0.0043 mm. This value was used in *Agisoft PhotoScan* (see Section 3.4.1).

(a) Setup of a GCP using a metal pole, red cardboard and a CD (D'Oleire-Oltmanns et al. 2012: 3398)

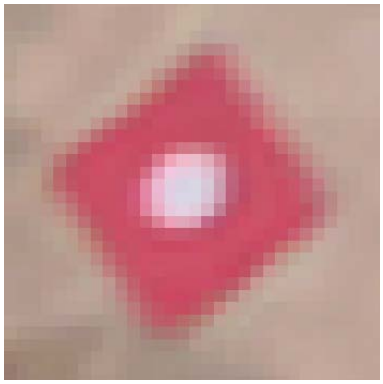

(b) GCP in aerial image from 105 m

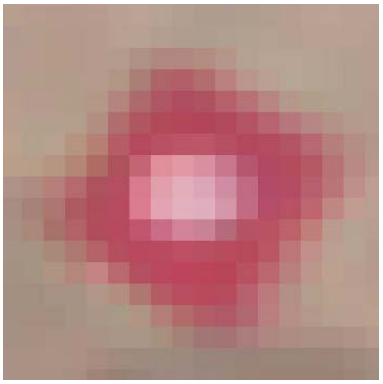

(c) GCP in aerial image from 190 m

Figure 3.2.: Visbility of GCPs at different scales

3.3. Data Acquisition

Using the flightplanning software MAVinci Desktop, the UAV was set to capture the area three times during one flight: once from a height of 85 m. This was directly followed by another flight from the same height in rotated path orientations and finally by a flight from a height of 170 m above ground. The height above ground was later calculated using the conventional and the SfM-approach. Both calculations resulted in an effective average flying height of approx. 105 m, respectively 198 m, which is 20–30 m more than configured. A total number of 531 images was taken during this flight. All images used were taken within approx. 15 minutes. Limited by the flight paths and possible turning maneuvers of the UAV, only virtually orthogonal images of the area of investigation were taken.

3.3.1. Ground Control Points

As stated in Section 2.2, external orientations or GCPs are not necessary for creating models using SfM. Nevertheless, for referencing the model it is common to capture GCPs using high accuracies. A total number of 30 GCPs was used in this study. They were marked and measured in the field by D'Oleire-Oltmanns et al. (2012: 3396) using metal poles, a red cardboard with the size of 30×30 cm and a Compact Disc (CD). This setup is easily identifiable and visible in aerial images at various scales (see Figure 3.2). The GCPs were measured using a total station and a local coordinate system. The precision for these measurements was estimated to approx. 0.5 cm for x/y and 1 cm for z-directions (D'Oleire-Oltmanns et al. 2012: 3397). Additionally, the GCPs were measured using a standard GPS unit, since official survey points for connecting the local coordinates to the national reference system were not available nearby (D'Oleire-Oltmanns et al. 2012: 3397).

3.3.2. Datasets

Four different sets of images were chosen to generate seven different DEMs (see Table 3.1). The reference-DEM was created using *Leica Photogrammetry Suite* and a selection of 58 images from

Table 3.1.: Datasets used for the SfM-approach and specific characteristics

ID	short name	images [count]	resolution [cm/pix]	point density [points/m^2]	points [count]	DEM size [pix]
SfM01a	LPScompare	58	4.6	479.8	40,913,119	6,381×7,949
SfM01b			10	120.0	10,121,430	2,911×3,630
SfM02a	LPSvalidation	50	4.4	511.7	38,203,374	6,398×7,252
SfM02b			10	127.9	9,467,241	2,827×3,205
SfM03	dense	108	4.5	494.2	48,759,918	6,616×8,112
SfM04	multiscale	260	6.1	269.4	35,357,203	6,063×6,243

the altitude of 105 m. The two DEMs listed as SfM01a and SfM01b use the same images as the LPS-model. The purpose of this dataset was to directly compare quality and derived hydrographic features from both methods. Since the optimum spatial resolution in LPS was proposed to be 10 cm, the same resolution was used for the SfM-approach (SfM01b). The quality setting for dense point cloud generation in *Agisoft PhotoScan* was set to medium, which resulted in a ground resolution of 9.1 cm. The DEM was resampled to a spatial resolution of 10 cm using the nearest neighbor assignment. In order to determine what's possible using SfM-techniques, the highest possible spatial resolution for this set of images calculated by *Agisoft PhotoScan* was used for SfM01a (4.6 cm/pix).

The 50 images for SfM02a and SfM02b were selected in order to validate the LPS-DEM using different images and a different method. Therefore, these images are different to those used for LPS-DEM-generation, yet, they were taken from the same altitude (105 m). Similar to SfM01, two spatial resolutions were calculated: 4.4 cm/pix and 10 cm/pix. SfM03 uses all 108 images from SfM01 and SfM02. The hypothesis to be tested using this dataset is that increasing the density of the images taken improves the quality of the DEM. Finally, SfM04 aims at improving the quality using images from different altitudes (scales). Therefore, all images from SfM03 and additionally all images from 190 m were selected for this dataset. This totals to an amount of 260 images and an average resolution of 6.1 cm/pix.

3.4. Data Processing

For creating the DEMs, the selected sets of images were processed using *Agisoft PhotoScan 1.1.6*. For qualitative and quantitative validation purposes and hydrologic analysis, *ESRI ArcGIS 10.2.2* was

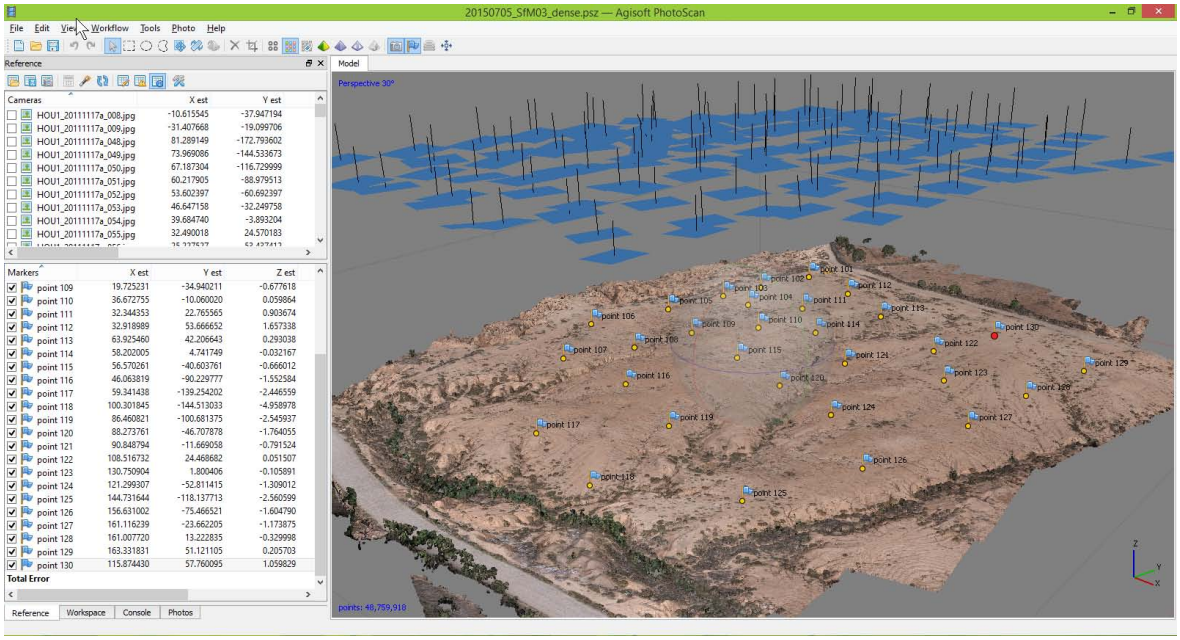

Figure 3.3.: Screenshot from *Agisoft PhotoScan 1.1.6* showing model SfM03 (left: reference pane including estimated coordinates and errors, right: colored dense point cloud with GCPs and visualization of estimated camera locations)

used, including the extensions *Spatial Analyst* and *ArcHydro*. The steps performed and the settings made in these software packages are described in the following sections. *Leica Photogrammetry Suite* (now known as *IMAGINE Photogrammetry*) is a common software application for photogrammetric analyses. Since it was not part of this thesis to generate the LPS-model, software-specific details are not described here, but it is referred to Chapter 2.1 for more details on photogrammetry in general.

3.4.1. Structure-from-Motion using Agisoft PhotoScan

The company *Agisoft LLC* was founded in 2006 and releases the photogrammetric software *Agisoft PhotoScan* for 3D reconstruction, visualization, surveying and mapping. The software is based on SfM-MVS-technology and reconstructs 3D-surfaces or models from multiple images. After importing the images into the software, the workflow consists of five major steps, which are described in the following sections: the alignment of images, the setting of GCPs, the generation of the dense point cloud, the calculation of a mesh and finally the export of DEMs.

Aligning Images and Camera Calibration

At first, the known camera parameters need to be set in the camera calibration window. The camera type was set to *Frame* and the pixel size – thus the physical dimension of one pixel on the sensor of the digital camera – was set to the calculated value of 0.0043 mm.

Since the images are not linked to geographic coordinates, they are not displayed in the main window after import. *Align photos* performs a quick referencing of the images by matching distinct points (key points) in adjacent images. A maximum number of 40,000 key points per image was

Table 3.2.: Camera calibration parameters, calculated in self-calibration process (principal point offset in mm, focal length in mm and distortion coefficients)

	SfM01	**SfM02**	**SfM03**	**SfM04**
total principal point offset (mm)	0.099	0.094	0.078	0.102
f_x **(mm)**	19.10	19.42	19.45	19.35
f_y **(mm)**	19.13	19.45	19.48	19.38
K1	-0.0243	-0.0254	-0.0254	-0.0255
K2	0.0404	0.0488	0.0470	0.0469
K3	-0.0215	-0.0410	-0.0354	-0.0313
P1	-0.00075	-0.00067	-0.00074	-0.00068
P2	0.00034	0.00064	0.00047	0.00040
skew	2.41	3.01	2.99	1.90

chosen. The maximum number of matches (tie points) was set to 20,000 per image to speed up the process. A sparse point cloud was built by estimating the camera positions and camera calibration parameters using the tie points. The accuracy was set to *High*, which means that the original images were not scaled before processing.

During this process, not only the external parameters are determined, but also the internal ones – the so-called self-calibration of the camera. These are the focal length in x- and y-dimension (f_x, f_y), the principal point coordinates (c_x, c_y), the skew transformation coefficient, which describes the angle between the X- and Y-axis of the pixels ($skew$), three radial distortion coefficients (k_1, k_2, k_3) and two tangential distortion coefficients (p_1, p_2). Table 3.2 lists all parameters calculated during the self-calibration procedure in *Agisoft PhotoScan* for the SfM-models.

Setting of Ground Control Points

The next step is the setting of the coordinates for the visible GCPs in all images. Each GCP needs to be marked in the images, labeled and provided with coordinates. *Agisoft PhotoScan* assists the user by automatically identifying GCPs that could be aligned using the sparse point cloud. Nevertheless, all GCPs need to be checked and repositioned accurately (see Figure 3.2). There are some reference settings that need to be made. According to D'Oleire-Oltmanns et al. (2012: 3397) the marker accuracy was set to 0.5 cm. The projection accuracy – the assumed accuracy of markers on the images – was set to 0.1 pix, since the good visibility of the GCP-targets allows for a quite accurate placing of markers. In *Agisoft PhotoScan*, the total number of visible GCPs in all images is called *GCP projections*. This value varies corresponding to the number of images used in each dataset between 141 for dataset SfM02 and 836 for SfM04.

Unlike described for the traditional SfM-approach (see Section 2.2), where GCPs are not used for

camera alignment, the previously estimated in- and external camera parameters can be optimized using the GCPs. This step accounts for possible non-linear deformations and adjusts the sparse point cloud and camera parameters by "minimizing the sum of reprojection error and reference coordinate misalignment error" (Agisoft LLC 2014: 35).

Dense Point Cloud Generation

As soon as the extent – for which the dense point cloud should be calculated – is set up correctly, the dense point cloud generation can be started. The quality of the calculation was set to *High*. This means, the images are downscaled by the factor of 4 before processing. The resulting resolution was approx. 4.5 cm/pix for images from a height of 105 m. This option was proposed by *Agisoft*, since – according to them – the *Ultra High* option is only suitable for very sharp images from close distances and not for aerial images. The depth filtering mode was set to *Mild*, the softest of three options, where small details will be preserved and not filtered out as noise.

Mesh Building

The dense point cloud needs to be interpolated in order to retrieve height information from any given point. As the surface type the option *Height field* was selected, because this option is optimized for planar surfaces and aerial images. The polygon count was set to *High*, which means that the number of polygon faces equals 1/5 of the number of points in the dense point cloud. In order to fill small holes within the mesh, interpolation was enabled.

Export of DEMs and Orthophotos

Finally, the actual DEM was exported using the "Export TIFF"-feature in *Agisoft PhotoScan*. Invalid parts of the DEM – visible on two images or less – were cropped. The pixel size for the output file was used as proposed. The recommended value is dependent on the quality setting during the dense point cloud generation. The TIFF-files have a filesize between 30 and 161 MB depending on their resolution and the area of coverage.

Agisoft PhotoScan also offers the export of a stitched and orthorectified aerial image of the entire area. This export was carried out using the SfM04-model, as this model uses most images and was assumed to be most precise. Compared to the orthophoto derived from the LPS-model, the differences in horizontal position accuracy are very low and negligible for visualization and manual digitalization.

3.4.2. Statistical and Hydrologic Analysis

Prior to the actual hydrologic analysis, some statistical comparisons have been drawn to assess the general quality of the DEMs. This statistical analysis was done using the reports provided by *Agisoft PhotoScan* and LPS. These reports include – amongst others – the estimated flying altitude, ground resolution, error values, point densities, numbers of projections and camera calibration parameters.

Additionally, the DEMs were subtracted from each other using the ArcGIS raster-calculator-tool and statistically analyzed to identify general differences between the models. All SfM-models were subtracted from the LPS-model and all SfM-models with comparable resolutions were subtracted from each other. The resulting raster-datasets were identically colored in 13 classes for better comparison. Additionally, minimum, maximum, mean and standard deviation values for each resulting raster were calculated.

Generating Drainage Networks

Hydrologic analysis of the DEMs was performed using common procedures as described by – amongst others – Tarboton et al. (1991) and O'Callaghan and Mark (1984). The basic procedure is as follows: filling of sinks, calculating flow direction and flow accumulation and defining channels using an area threshold (Tarboton et al. 1991: 84).

The software used is *ESRI ArcGIS 10.2.2* including *ArcHydro* (version 10.2, March 2, 2015), a plug-in for ArcGIS that enables complex hydrologic applications. *ArcHydro* provides the data model for hydrologic networks and the necessary tools to calculate and analyze these. A *File-Geodatabase* was used to store the drainage networks. Using the *Model Builder* of ArcGIS, a model performing all necessary steps mentioned above was built. Since the areas of all DEMs exceed the selected area of investigation, the drainage networks were calculated for the total DEMs and finally clipped to the actual area of investigation to make them comparable. This allows the drainage lines to leave the area and re-enter it at a different point without being connected.

The first step is the filling of drainage sinks within the DEM to allow for a continuous flow from any given point. Depressions are filled up to the height of the lowest surrounding pixel. The resulting raster is used to calculate the flow direction for each pixel using the steepest descent from that pixel. The general concept of defining the flow direction for each cell was initially described by Marks et al. (1984). ArcGIS uses a method called D8-model, according to the concept of Jenson and Domingue (1988) that is commonly used nowadays. Despite the common use, the applicability of this method is discussed vigorously, since only one drainage direction is possible (see Wechsler 2007: 1484). Nevertheless it was used here, since it is commonly utilized in hydrologic applications and it was not the aim of this work to accurately identify streams. The possible eight directions (E, SE, S, SW, W, NW, N, NE) are coded as values between 1 and 128. The flow direction raster is then used to calculate the flow accumulation, calculating the amount of pixels that drain into each pixel.

The next step is the definition of streams. The most common procedure is using an accumulation threshold that defines a drainage area below which a drainage line may be assumed. How to define these thresholds is discussed in hydrology and several studies propose different approaches (Bhowmik et al. 2015; Vogt et al. 2003). The aim of this work is not to accurately derive channel networks from high resolution DEMs, but to validate DEMs using common hydrologic approaches. Therefore, the visually most suitable threshold was chosen by testing different values. In this case, an accumulation threshold of 20 m^2 was selected. This area had to be converted to the equivalent number of pixels according to the resolution of each raster, since the input for the tool needs to be expressed as a number of pixels.

The tool *Stream Segmentation* assigns a unique value to each segment between two segment junctions and to each head segment using the flow direction and the stream rasters. Similar to this, the tool *Catchment Grid Delineation* assigns the same value to the corresponding watershed for each segment. The *Catchment Polygon Processing* function converts these areas into vector data joining neighboring pixels with the same values. Correspondingly, the tool *Drainage Line Processing* converts the stream raster to vector features assigning the raster ID of each stream segment to the vector features. *Adjoint Catchment Processing* creates one aggregated upstream catchment polygon for each catchment that is not a head catchment. This dataset is used to speed up the following processes. *Drainage Point Processing* determines one drainage point for each catchment area. Finally, the tool *Hydro Network Generation* converts the drainage features into network features, connecting all relevant features using IDs, setting correct flow directions and creating unique *Hydro Junction* features.

Comparing Drainage Networks from different DEMs

To compare the drainage networks, the following approach was chosen: A buffer was drawn for each network (e.g. LPS) and substracted from the other networks that needed to be compared to these (e.g. SfM04). The result is a set of line features that represent the parts of a network that lie outside the buffer size of the source network and were considered to be only present in the subtracted network and hereafter termed with the suffix *only* (e.g. SfM04_only).

The buffer size was chosen systematically by manually digitizing the maximum distance between drainage lines that were assumed to belong together using line features. A total number of 400 samples – scattered across the area – was collected. The statistics of these features (Table 3.3) were used to find an optimum buffer size. Since the median (0.22 m) would exclude half of the selected samples, the 3-rd quartile (0.29 m) was rounded (0.3 m) and used as the buffer size. This includes more than 75 % of all measured widths. The results after subtracting the networks were visually plausible. However, using this method, drainage lines crossing at right angles are considered the same for the width of the buffer (see Thommeret et al. 2010: 1532). This characteristic is not very likely to happen at all, since the major features of the DEMs are the same, and thus neglected in this study.

Table 3.3.: Statistical values of the sample data for the determination of the ideal buffer size

Minimum	Mean	Median	3-rd Quartile	Maximum	Count
0.05 m	0.23 m	0.22 m	0.29 m	0.52 m	400

Manually Validating Drainage Networks

In order to get an idea of how accurate the derived drainage networks are compared to a manually digitized channel network from aerial images, three validation-areas (VA1–VA3) were chosen and all channels within these were digitized (see Figure 4.17 on page 35). To refine these channels, an

attribute was set describing three types of channels: shallow, deep and assumed. Deep channels are characterized by steep slopes and sharp edges. They are clearly specifiable. Shallow channels mostly have soft slopes and they are harder to identify. Assumed channels are not visible and mostly hidden under vegetation or in tunnels. They still can be identified by obvious in- and outlets.

Three subareas were selected to reflect three different types of drainage networks within the area of investigation: The north-eastern part is – due to the anthropogenic influence – characterized by shallow rills and mostly featureless terrain (VA1; 1,234 m^2). The central part is characterized by incised gullies and little vegetation (VA2; 3,014 m^2) and the south-western part is covered with deeply incised and wide gullies with a lot of shrubs (VA3; 2170 m^2). The digitized drainage networks were compared to the drainage networks derived from LPS and SfM04-DEMs using the same approach as described in Chapter 3.4.2.

Comparing Watershed Areas

To get an impression of the hydrologic accuracy of the DEMs, sub-watersheds were analyzed, too. In order to perform this analysis, the intersections between three drainage networks (LPS, SfM03 and SfM04) were calculated using the tool *Intersect* in ArcGIS. A random selection of 100 intersections was made by adding random numbers to each point, sorting them by this value and selecting the first 100 points. These points were snapped (within the distance of one raster cell size) to the cell with the highest flow accumulation for each DEM (*Snap Pour Point*). This procedure was necessary to allow for the highest possible position accuracy while using three different cell sizes (10; 4.5 and 6.1 cm). Since two of the initial pour points were only 14 cm apart, these points snapped to the same pour point on the LPS-raster. Thus, only 99 pour points could be used for the calculation of the LPS-watersheds. The ArcGIS-tool *Watershed* was used to calculate the watersheds for each individual pour point in all three models. The results were two rasters with 100 and one raster with 99 watershed-areas, each identified by the pour-point-ID. These rasters finally have been vectorized.

To calculate the differences and similarities between the watersheds from all three models, they were blended using the *Union*-tool in ArcGIS. The LPS-watersheds were compared to SfM03, SfM03 to SfM04 and SfM04 to LPS. The outcome was one dataset for each combination, containing polygons that could be nonambiguously attributed to one of the following categories: identical pour point for both models, different pour points for both models, watershed only in one model.

4. Results

The analysis consists of three major parts: First of all, the qualitative analysis is performed by visually interpreting and evaluating the generated DEMs and drainage networks. The next step is a short quantitative analysis, which aims at statistically comparing the results. Finally, the focus is brought to the main part of this work: the hydrologic analysis of derived drainage networks and watersheds. All results are presented in the following sections.

4.1. Digital Elevation Models

The digital elevation models were imported in ArcGIS and transformed to a colored, shaded relief map for visually interpreting the surface. In the following passages, the term "SfM01", etc. refers to these shaded reliefs and not to the actual DEM. Furthermore, it needs to be considered when reading the following passages that the tilted north arrow in all maps indicates that they are not oriented.

The DEM (e.g. Figure 4.3) is characterized by two main channels that cross the area from north-east to south-west. These gullies have their origin within the area and start with branches at sub-meter scale and leave the area at a width of several meters. The area appears to be sloped from north-east to south-west causing the runoff to follow this direction.

Apart from these main characteristics, there are some noticeable details. The eastern part of the area is separated by a linear feature that looks like an artifact. This is in fact the result of anthropogenic influence. This part has been leveled several times to fill the emerging gullies. In the northern part, there is a line of approx. 13 small bumps with a diameter of roughly 4 m. These are piles of gravel that were discharged there for the future construction of a road. Finally, there is an exposed rectangular feature in the north-eastern corner of the area. This is the minibus that was used to transport the equipment, which is an excellent example to demonstrate the differences of the models (Figure 4.1).

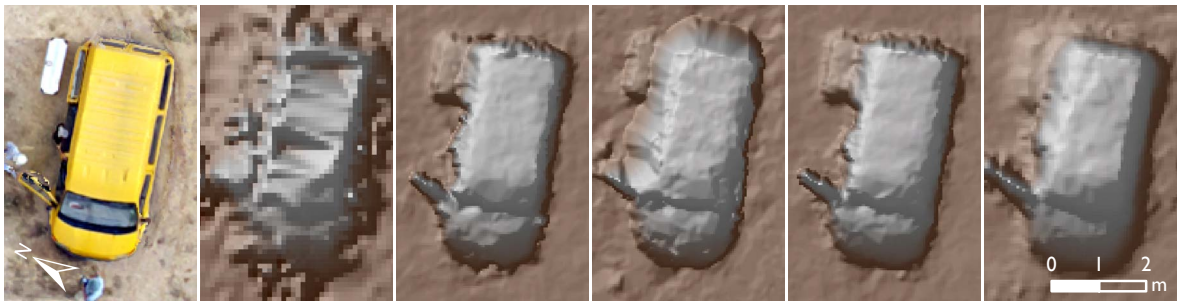

Figure 4.1.: Examples from shaded and colored DEMs (from left to right: orthophoto, LPS, SfM01a, SfM02a, SfM03, SfM04)

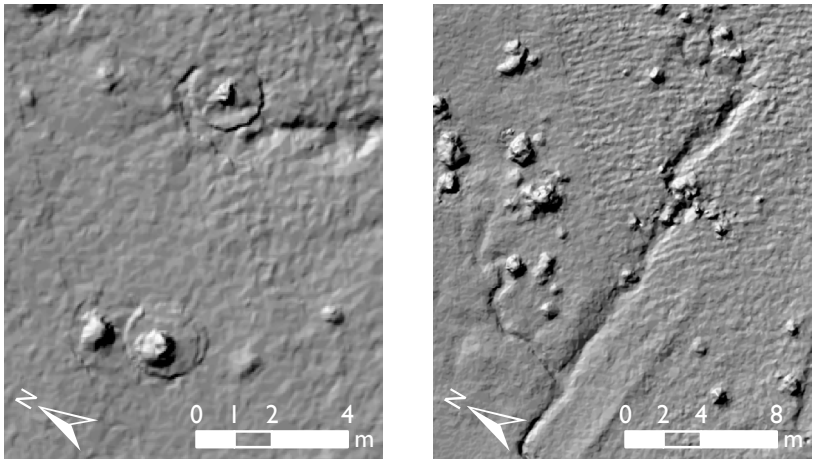

(a) Small, circular and elevated artifacts, mostly visible around shrubs

(b) Extensive, wavelike artifacts with concentric circles

Figure 4.2.: Examples for artifacts visible in SfM01a (different scales)

SfM01a and SfM01b (Figure A.1 and A.2, page 50 f.) appear to be pretty smooth with a high amount of detail and no obvious errors. At the second glance, some artifacts may be identified. SfM01a contains some small circles (2–3 m) mostly around bushes in the top right corner of the area (example in Figure 4.2a). The image overlap here was between four and six images which is not too bad. Secondly, there are some wavelike artifacts consisting of sections of concentric circles. These artifacts are delimited by straight lines marking the abrupt transition between areas with artifacts and those without (example in Figure 4.2b). At the lower resolution of 10 cm, SfM01b does not show the small circles, but the same wavelike artifacts in the same areas – slightly smoother due to the lower resolution.

The shaded reliefs of SfM02a and SfM02b (Figures A.3 and A.4, page 52 f.) give the same overall impression as SfM01. The overall number and intensity of artifacts and noise is slightly increased. However, the circles described for SfM01a could not be observed at all. Only the wavelike artifacts were present throughout the whole DEM.

The third model, SfM03 (Figure A.5, page 54), gives a better impression. The overall noise is immensely reduced compared to the previous models (see Figure 4.1). Circular artifacts can only be observed in the outmost corners of the model, which is outside the actual area of investigation. This area has an image overlap between two and three images.

Model SfM04 (Figure 4.5) has the highest redundancy of images with an overlap of nine images at nearly any given point. The DEM generated using this model almost does not show any of the artifacts mentioned above. The general noise is highly reduced, there are no holes in the DEM that needed to be filled with TINs – as it was the case for the LPS-model – and straight lines due to bad transitions between clusters are not visible at all. Still, due to the lower resolution of 6.1 cm, the visibility of small details is reduced (see Figure 4.1).

Since the LPS-DEM serves as a reference for all SfM-models, it is described here as well. Three types of obvious irregularities can be detected in this DEM: The general noise (Figure 4.4a) can be noticed throughout the whole model. It is probably caused by bad image quality and the algorithms

used within *Leica Photogrammetry Suite*. Secondly, larger shapes formed like triangulated irregular networks (Figure 4.4b) indicate low point densities due to the lack of images or identifiable tie points. These areas had to be interpolated, which results in erroneous surfaces. Finally, straight lines (Figure 4.4c) crossing the whole DEM indicate areas where point clusters from different images or bundles could not be perfectly aligned. This may be caused by bad image overlap.

Visually comparing the shaded reliefs of the LPS-DEM (Figure 4.3) with the SfM-DEMs reveals some obvious differences: All variations of the SfM-model seem to have less noise. The surface of all SfM-models appears to be smoother with less irregular bumps and roughness. This can also be observed using the example of the minibus (see Figure 4.1). The LPS-model (second from left) has large irregularities and obviously enormous problems reconstructing the roof of the car. The SfM-models are – from left to right – increasingly better in reconstructing the minibus, although SfM04 (far right) has slightly less distinct edges due to the lower resolution (6.1 cm). Nevertheless, it has to be taken into account that the car has a reflecting surface and this example may not be used to quantify the overall performance of the SfM-technique.

The GCP-errors in all three dimensions (X-, Y-, Z) and total errors were used to compare the models (Table 4.1). The variations of models SfM01 (SfM01a and SfM01b) and SfM02 (SfM02a and SfM02b) use the same images and alignments. Therefore, the error values are the same and not listed here twice.

The model SfM04 has the smallest total error (2.8 cm), although the Y- and Z-errors are smaller (by 0.03 respectively 0.11 cm) for model SfM01 respectively SfM02. The latter model has the largest total error (3.26 cm) and the largest errors in X- and Y-dimensions. Regarding the GCP-errors, this model performed worst. The LPS-model has the second smallest total error value (3.07 cm) and medium to high X-, Y- and Z-errors. Models SfM01 and SfM02 have total error values of 3.1 respectively 3.26 cm. While SfM01 performed well in X- and Y-dimension, SfM02 performed worst in these directions, but best in Z-direction. GCPs for SfM03 have a total error of 3.09 cm and – compared to the others – medium error values in X-, Y- and Z-directions.

The variations of the Z-error are plotted as boxplots in Figure 4.6. The LPS-model has the largest total variation (maximum and minimum between -16 and 10 cm) and the largest interquartile range. The variations of the SfM-models are significantly smaller. The variation of SfM04 is smallest, although SfM02 and SfM03 are similar. SfM01 performs slightly worse, but still better than the LPS-model.

Figure 4.7 (left) illustrates the correlation between the number of GCP projections, which is the number of all GCPs visible in all images, and the RMSE of the GCPs. Model SfM04 has, due to the high number of images used (260), a total amount of 836 GCP projections. Simultaneously, as stated above, the total error value is the lowest for this model. In contrast, the model with the highest error value (SfM02) has the lowest amount of GCP projections. For illustration purposes, a linear trend line has been drawn into the diagram (Figure 4.7). The diagram on the right hand side illustrates the number of GCP projections versus the total reprojection error. In this case, the trend is inverted: Model SfM04 has the highest amount of GCP projections and also one of the highest reprojection errors (0.82 pix).

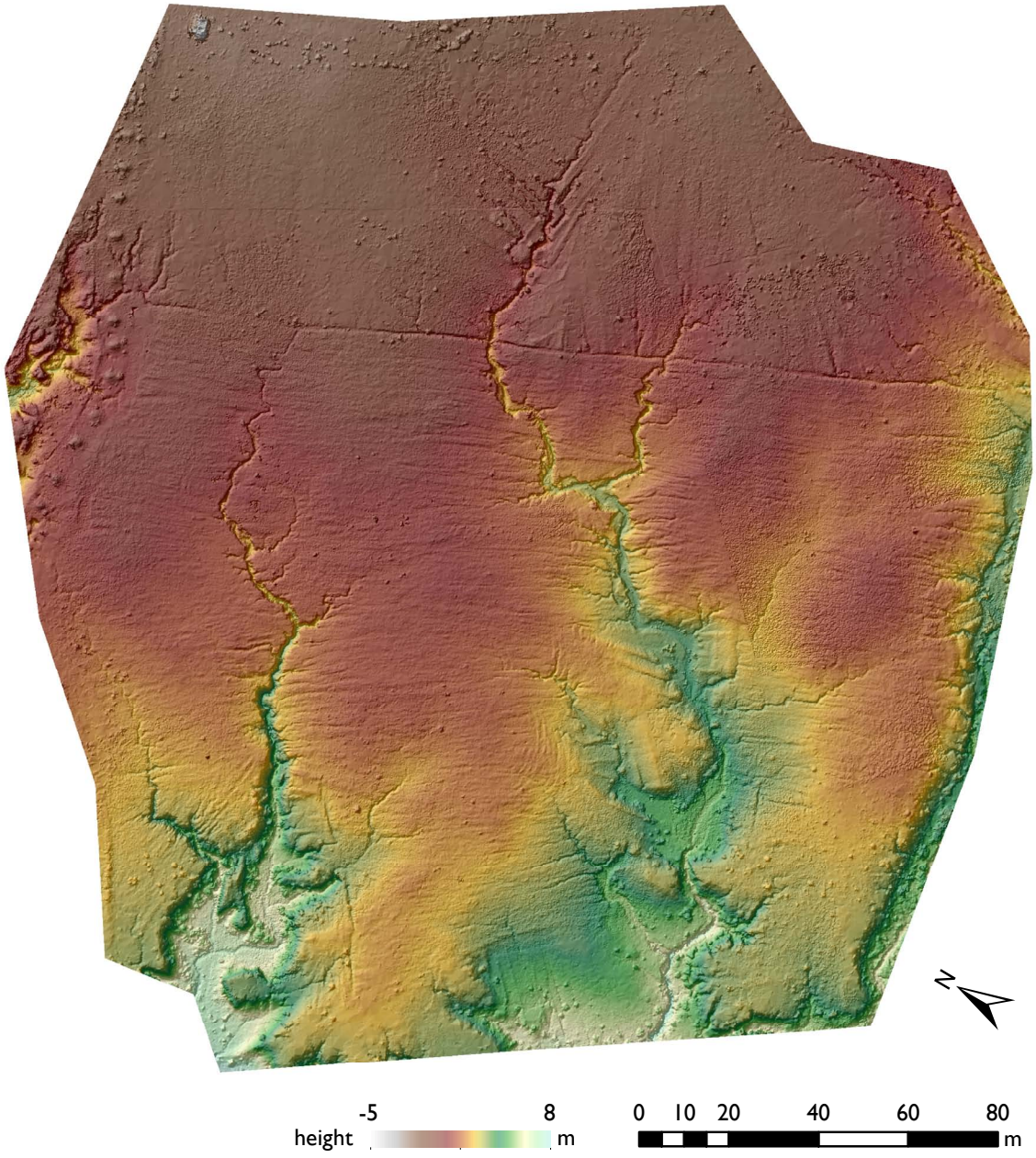

Figure 4.3.: Shaded and colored relief of the LPS-DEM (resolution: 10 cm)

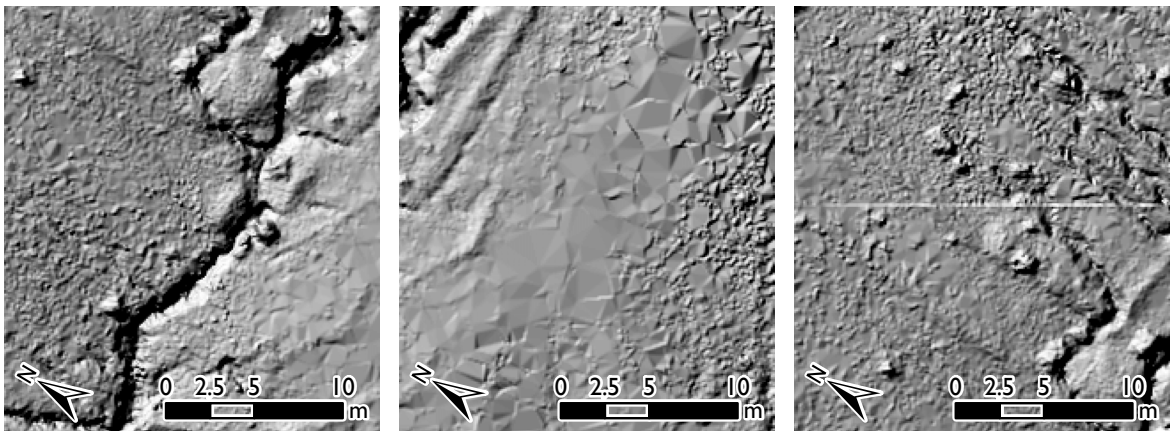

(a) General noise (b) TIN-artifacts (c) Horizontal, straight line

Figure 4.4.: Examples for artifacts visible in the LPS-model

Table 4.1.: Total GCP-errors for each model (cm), separately for each dimension (X, Y, Z) and the reprojection error (pix)

	LPS	SfM01	SfM02	SfM03	SfM04
X-error (cm)	1.87	1.67	1.89	1.76	1.65
Y-error (cm)	1.55	1.48	2.15	1.81	1.51
Z-error (cm)	1.88	2.15	1.56	1.77	1.67
total error (cm)	3.07	3.10	3.26	3.09	2.80
reprojection error (pix)	0.41	0.66	0.55	0.83	0.82

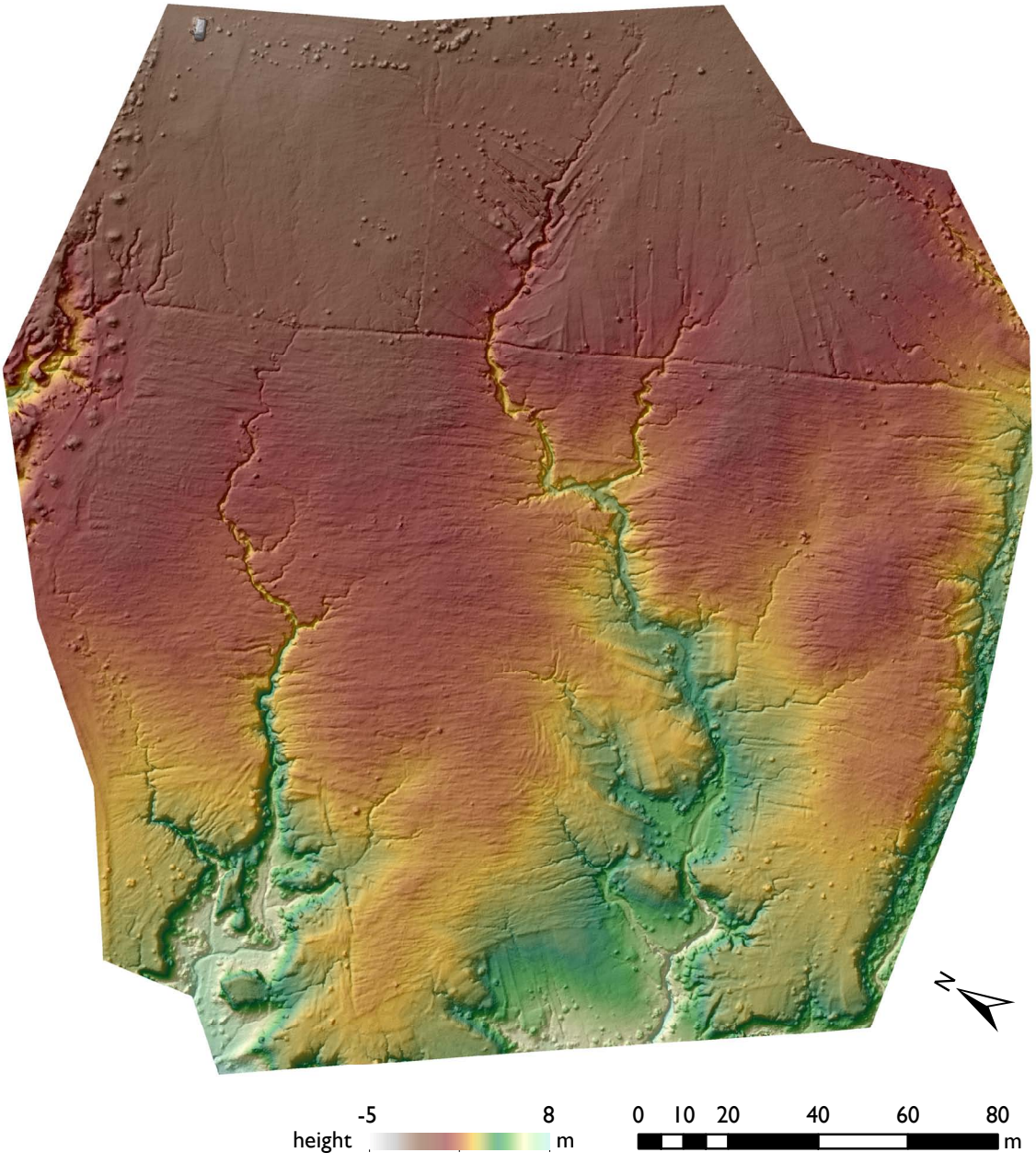

Figure 4.5.: Shaded and colored relief of the SfM04-DEM (resolution: 6.1 cm)

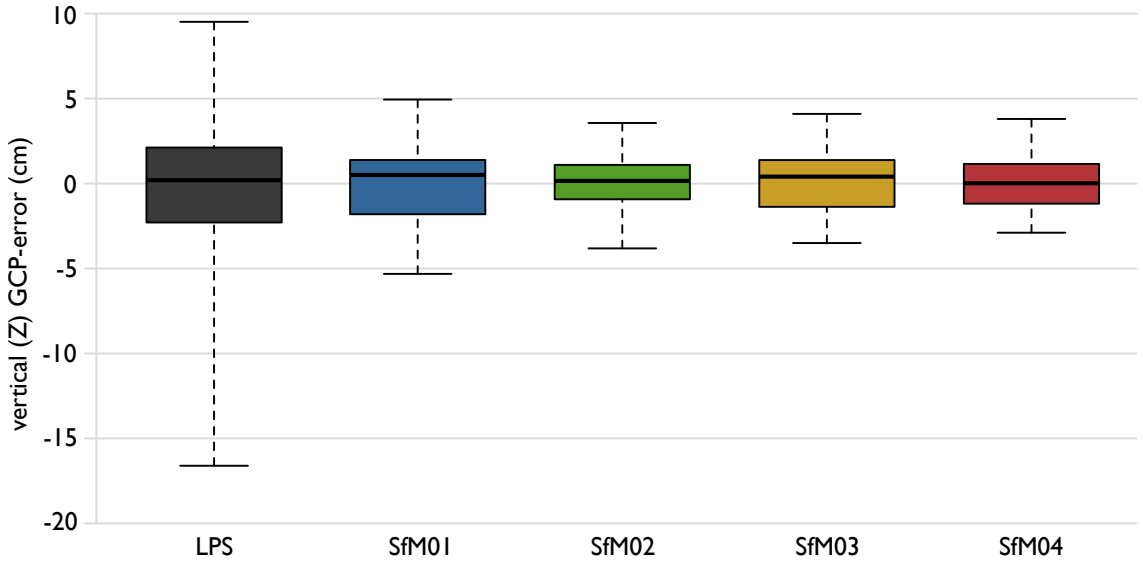

Figure 4.6.: Boxplots for vertical GCP-errors (LPS: n=29; SfM: n=30) for each model (values top down: maximum, 3rd quartile, median, 1st quartile, minimum)

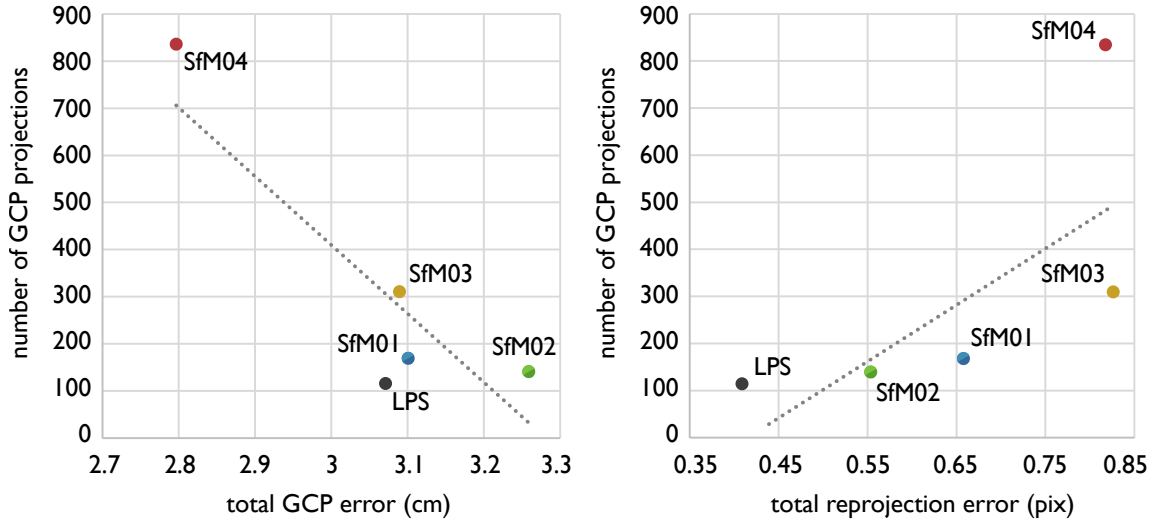

Figure 4.7.: Number of GCP projections versus RMS GCP error (left) and number of GCP projections versus RMS reprojection error (right)

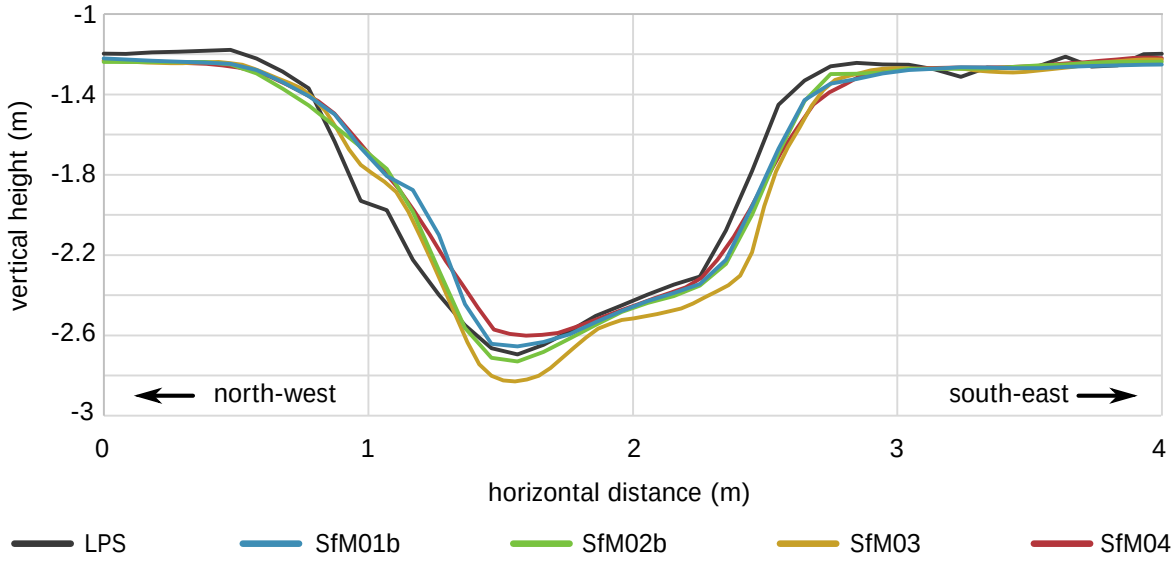

Figure 4.8.: Comparison of DEM-height profiles for a section of 4 m

4.2. Differences Between DEMs

Not only the raw DEMs were analyzed, but also the differences between the DEMs. The rasters of all calculated differences reveal straight edges scattered across the whole raster (see Figure 4.9). These artifacts reflect the positions of the original images. They are small enough (few centimeters) to be invisible in the shaded relief. Another issue can be seen in Figure 4.9: The resulting rasters of the comparison between the LPS and the SfM-models all show some sort of doming effect. This means that the differences of the DEMs are mainly positive in the center and negative at the corners. This does not apply to the differences between the SfM-models themselves, where there is no clear trend that may indicate this doming effect.

The rasters of the differences between the LPS- and the SfM-DEMs (e.g. LPS minus SfM04 in Figure 4.9) feature some distinct characteristics: The main gully lines are represented by parallel blue and orange lines. The orange part – which stands for negative values, meaning that the LPS-DEM was lower in this areas – is always on the north-western side, the dark blue parts constitute the opposite: higher areas on the south-eastern side. This effect is only visible for the differences between the LPS and the SfM-DEMs and was further analyzed by creating profiles for all DEMs and comparing them (see Figure 4.8). These comparisons revealed that the locations of the gullies are not shifted as it may be expected. The deepest point (the thalweg) is in fact mostly the same for these relatively large gullies. The reason for this characteristics is most likely that the walls of the gullies of the LPS-DEM have a different curvature. On the one side (mostly north-western), the level of the LPS-DEM is always below those of the SfM-DEMs. This results in a negative Z-value for the difference (e.g. LPS minus SfM04) and thus in the orange representation on the map. At the south-eastern wall of the gullies, the LPS-DEM is above the SfM-DEMs resulting in positive values and a dark blue color.

The overall statistical values (Table 4.2) for the differences between the SfM-DEMs and the LPS-

Table 4.2.: Standard deviation (top) and mean values (bottom) for differences between the SfM- and LPS-DEMs in cm

	SfM01a	SfM01b	SfM02a	SfM02b	SfM03	SfM04
LPS	8.50	7.99	7.70	7.63	7.66	7.48
	-2.24	-2.36	-0.19	-0.47	-1.02	-1.53
SfM01a			5.53		4.26	4.68
			1.88		1.12	0.52
SfM01b				5.36		
				1.89		
SfM02a					3.93	4.54
					-0.79	-1.42
SfM03						3.93
						-0.60

DEM show that LPS-SfM04 (read as: LPS minus SfM04) has the lowest standard deviation (7.5 cm), although LPS-SfM02a has the lowest mean value (-0.2 cm). The same images were used in the generation of LPS and SfM01b, and the same resolution was used to export the DEM. Nevertheless, the differences between those two models are the highest: the mean value for the difference between those two DEMs is -2.4 cm and the standard deviation is 8.0 cm. However, the mean value is not very robust against outliers and therefore not ideal for comparing similarities of different raster-datasets. Regarding the standard deviation, SfM03 and SfM04 are most similar (3.9 cm).

4.3. Hydrologic Analysis

The drainage networks derived from all DEMs were visually described and compared to each other and to the orthophoto derived from SfM04. The general overview (Figures 4.10 and 4.11) shows that there are two main channels from north-east to south-west that have a dendritic network. Many segments – especially at lower stream orders – are near-parallel and may be described as trellised (e.g. Jung et al. 2015: 41). These types of drainage systems are formed where structures, like tracks of bulldozers, guide surface runoff and subsequently the formation of gullies. The anthropogenic influence is especially visible in the north-eastern part, where the linear feature, also visible in the shaded relief (see Chapter 4.1), seems to be a barrier to the runoff and guides it to only five outlets. These are – with one exception – the same for all drainage networks.

Visually comparing the models (Figure 4.11) does not reveal any obvious differences. The main characteristics – as described before – are the same. Looking at the numbers (Table 4.3) reveals that the total lengths of all networks (clipped to the area of investigation) vary between 9,245 and 10,162 m (Figure 4.12a). Compared to the LPS-model, the drainage network of SfM01b is 9 % smaller (-918 m), which is the largest difference. Regarding the total length, SfM02a is most similar compared

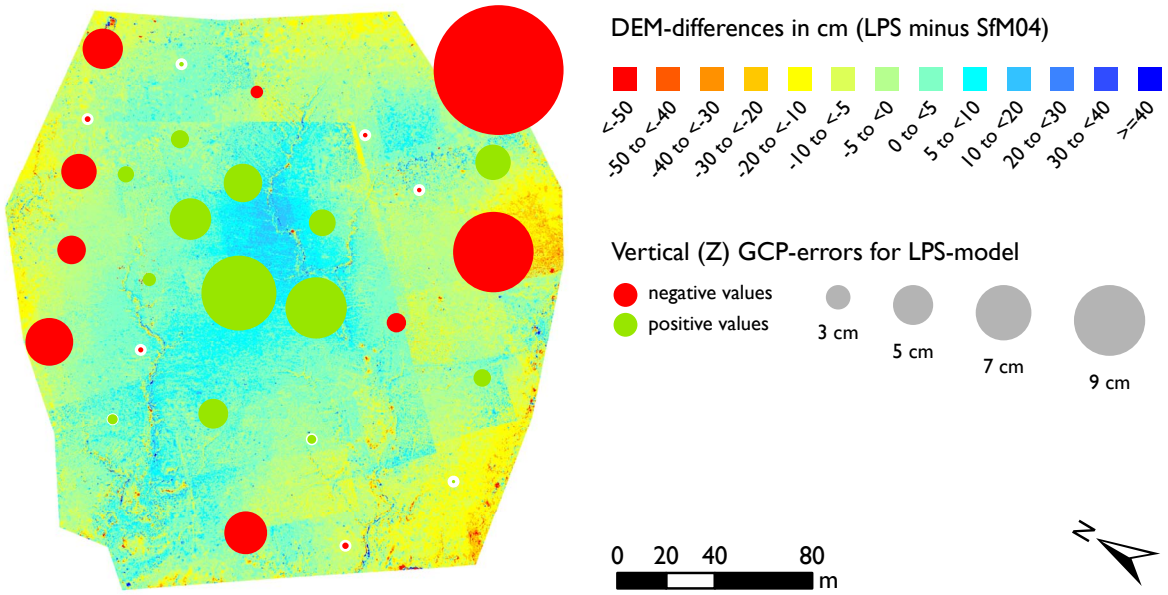

Figure 4.9.: Difference between the LPS- and the SfM04-DEM and the Z-error of the GCPs for the LPS-model. Small errors are highlighted with white circles.

to the LPS-model (total: 9,903 m; difference: -2.6 %), although the resolution of SfM02a is higher. Furthermore, all three models sharing the same resolution of 10 cm (LPS; SfM01b; SfM02b) have completely different total drainage network lengths (10,162 m; 9,245 m; 9,633 m). This suggests that there seems to be no correlation between the total length of the drainage network and the resolution of the DEM used.

Table 4.3 also lists the number of segments per drainage network. A segment is the drainage line between two junctions. This number only varies by a maximum of 63 (-4.8 % for SfM01a compared to LPS). Since the differences in total length are higher (up to 9 %), the reason must be that there are not only more but also longer segments. This is noticeable in Table 4.3 where the average length per segment seems to correlate with the total length of the drainage network. Another correlation can be observed in Figure 4.12b. Here, the correlation between the number of segments and the resolution of each model was illustrated using a linear trend line for illustration purposes. The lower the resolution of the DEM, the less segments seem to have been generated for the drainage network.

Using the orthophoto from model SfM04 as a reference, some more spatial details are revealed: There are areas where all drainage networks are very similar (e.g. Figure 4.13, left) and others where the divergence is much larger (e.g. Figure 4.13, center). The most obvious difference is that the areas with higher similarity are mostly characterized by deeply incised gullies.

Vegetation plays an important role in the generation of DEMs, too. The elevation models created are actually Digital Surface Models (DSM), since vegetation has not been filtered. This results in small humps where an unobstructed view to the ground was impossible due to shrubs. These humps are barriers to the surface runoff, causing drainage lines to meander around them (see Figure 4.13, center, upper part). Whether this is an problematic behavior or not has to be discussed.

The most eminent problems of the drainage networks are depicted in Figure 4.13 on the right hand

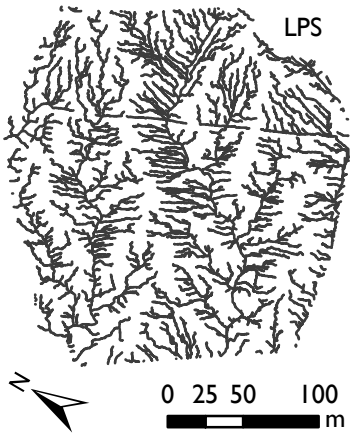

Figure 4.10.: Drainage network derived from LPS-DEM

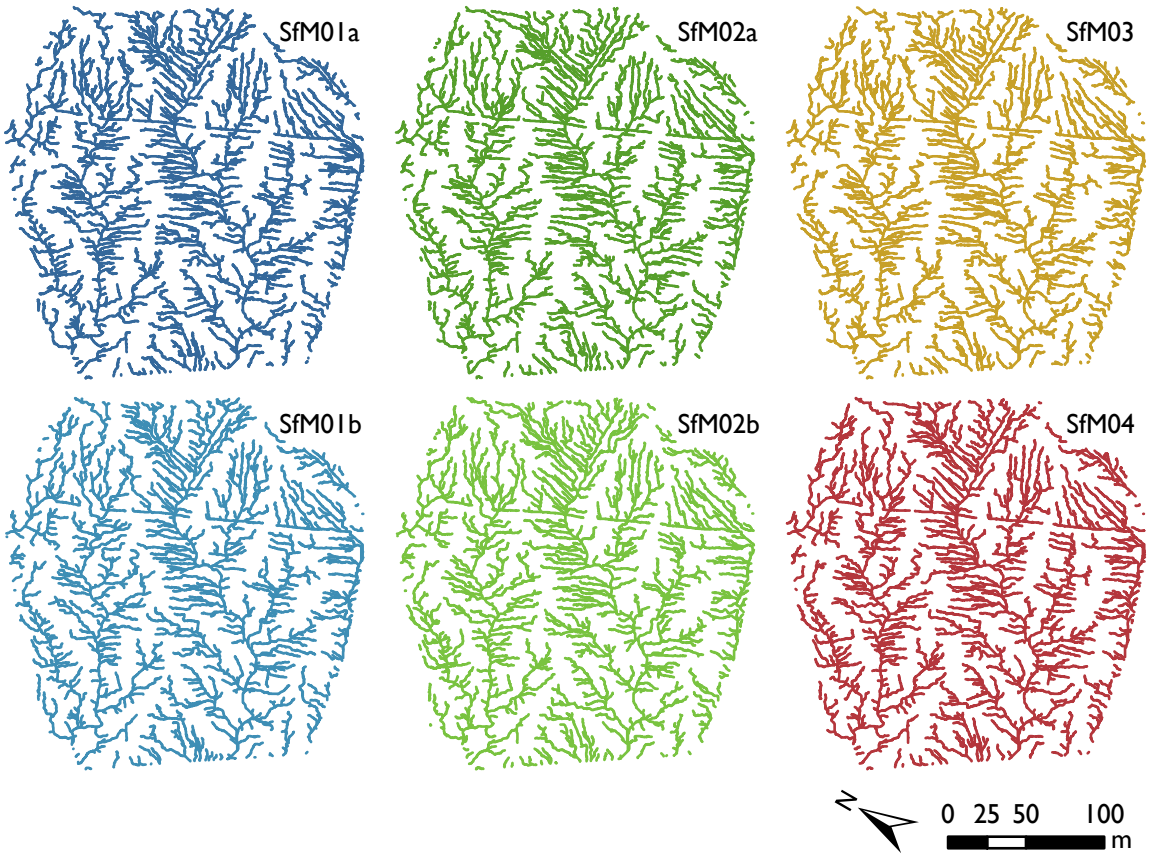

Figure 4.11.: Overview of drainage networks derived from SfM-DEMs

Table 4.3.: Statistics for drainage networks derived from DEMs (ASL: average segment length; DD: drainage density)

	resolution [cm]	total length [m]	difference to LPS [m]	[%]	segments [count]	ASL [m]	DD [1/m]
LPS	10.0	10,162.3	–	–	1,323	7.68	0.23
SfM01a	4.6	9,737.7	-424.5	-4.2 %	1,386	7.03	0.22
SfM01b	10.0	9,244.8	-917.5	-9.0 %	1,343	6.88	0.21
SfM02a	4.4	9,903.1	-259.2	-2.6 %	1,368	7.24	0.22
SfM02b	10.0	9,632.8	-529.4	-5.2 %	1,342	7.18	0.21
SfM03	4.5	9,712.8	-449.5	-4.4 %	1,379	7.04	0.22
SfM04	6.1	9,508.6	-653.7	-6.4 %	1,347	7.06	0.21

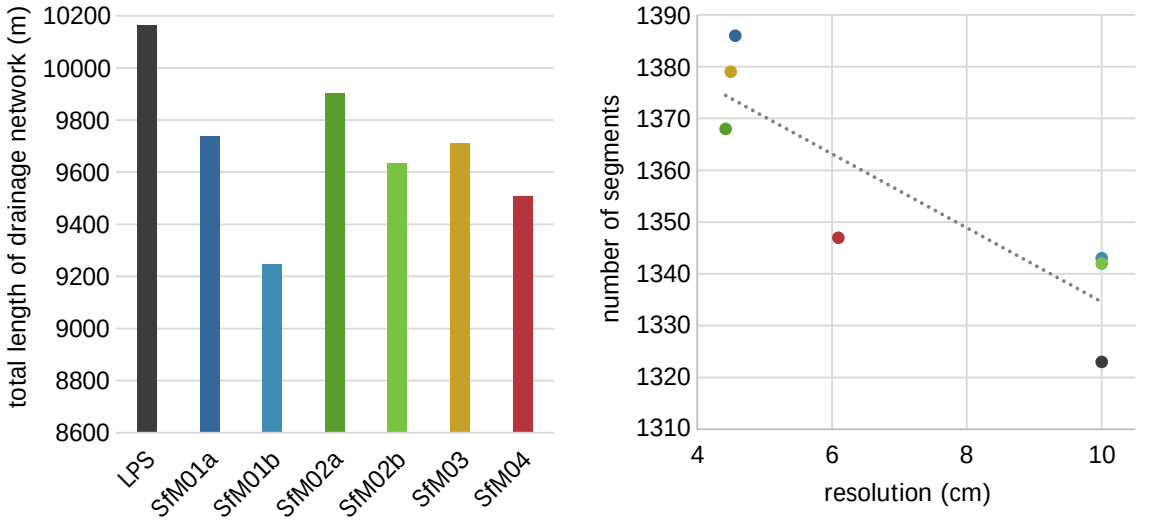

(a) Total lengths of drainage networks

(b) Correlation between resolution and number of segments

Figure 4.12.: Drainage network statistics

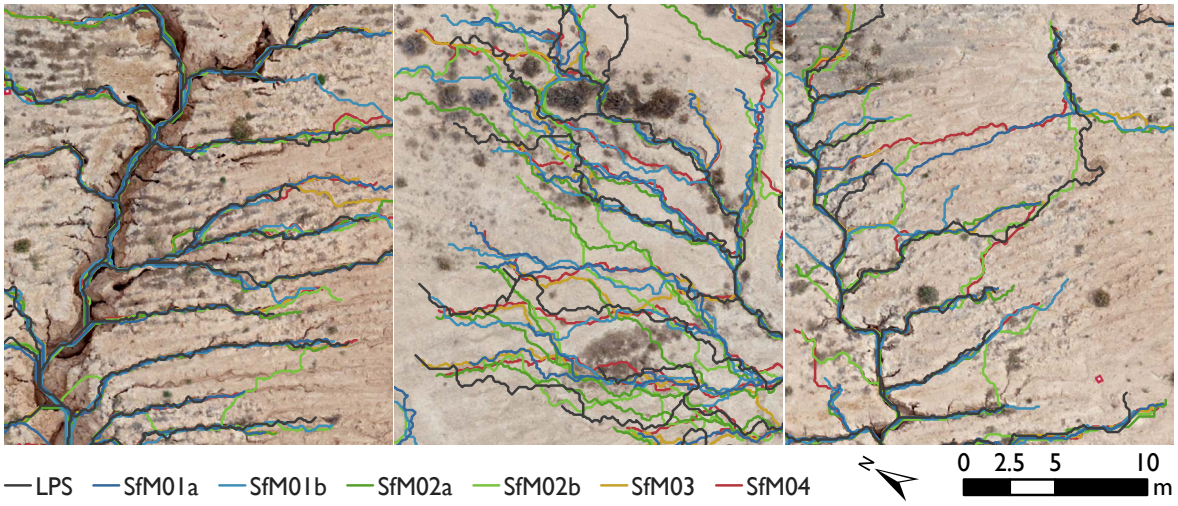

Figure 4.13.: Details of drainage networks using the orthophoto from model SfM04 as reference: good match in areas with incised gullies (left), poor match and influence of vegetation in flat and featureless areas (center) and totally differing runoff (right)

side. The drainage lines of all seven models start in the upper right corner of the image. After a few meters, they split in three different directions: SfM04 and SfM01a directly head north-west. SfM02b and LPS first head west and then follow SfM04 and SfM01a north-west. The remaining networks (SfM01b, SfM02a and SfM03) drain south-east in the opposite direction. This effect occurs several times throughout the whole area (approx. 10 times, depending on the level of detail looked at). This problem will also be further addressed when analyzing the watersheds.

4.3.1. Differences Between LPS- and SfM-networks

Figure 4.14 illustrates the drainage network of the LPS-model in dark gray and the SfM-only networks in corresponding colors. The SfM-only networks represent only those drainage lines that are different from the LPS-network. The north-eastern part seems to have more differences in the drainage networks, since more of the SfM-only drainage lines are visible. This was validated by dividing the area in two parts: a north-eastern part and a south-western part (see Figure 4.15a). Drainage densities for both areas have been individually calculated for the complete LPS-network, and each SfM-only network. All drainage densities are theoretical values that refer to what is visible in Figure 4.14. First of all, the total drainage density is higher in the north-eastern part (0.87 m/m²), compared to the south-western part (0.57 m/m²). But also the percentage of drainage density that is attributed to the SfM-only networks is higher in the north-eastern part (see Figure 4.15b): 72 % compared to 62 % in the south-western part. This proves the intuitive impression when examining the distribution in Figure 4.14.

Focusing on the whole area again, the percentages of the SfM-networks that are only present in these networks lie between 32 and 38 %. This equals a total length of 3,058–3,692 m. However, there are almost no differences between the SfM-models. All models sharing the higher resolution (<10 cm) have a proportion of 32 % that is only present in their drainage network compared to the

Table 4.4.: Differences between drainage networks (total amount and relative proportion of drainage line that is only present in SfM-networks)

	SfM01a	SfM01b	SfM02a	SfM02b	SfM03	SfM04
LPS	3,121 m 32 %	3,262 m 35 %	3,208 m 32 %	3,692 m 38 %	3,105 m 32 %	3,058 m 32 %
SfM01a			2,385 ,m 24 %		1,742 m 18 %	1,973 m 21 %

LPS-model. Network SfM01a was also compared to SfM02a, SfM03 and SfM04. Here, this proportion was substantially smaller (24 %; 18 %; 21 %).

Another property is illustrated in Figure 4.16. The percentages of the drainage networks derived from the SfM-DEMs that are identical to the LPS-derived network are plotted, differentiated by stream order. At the lowest possible stream order (head segments), between 50 and 60 % of the networks are identical to the LPS-network. The higher the stream order, the higher the amount of similarity. However, for SfM01a, SfM01b, SfM03 and SfM04, the highest stream order has a lower congruency (74–81 %) than the previous stream order (90–96 %).

4.3.2. Drainage Network Validation

The match between the drainage networks derived from the LPS- and SfM04-models and the manually digitized drainage networks (validation networks) was calculated. The overall match for SfM04 is slightly better (59 %) than for the LPS-network (56 %). All three validation areas and their locations within the area of investigation are depicted in Figure 4.17 and individually analyzed in the following paragraphs. The first validation area (VA1) is located in the north-eastern part where most of the drainage lines were label as shallow (92 %). Only 7 % of the digitized drainage lines were deeply incised. The similarity to both DEM-derived networks (SfM04 and LPS) is lowest in this area: only 40 % resp. 32 % of the DEM-derived networks match the validation network (Table 4.5).

The second validation area (VA2) lies in the central part of the area and is characterized by deeply incised gullies (67 %), shallow gullies (30 %) and only little vegetation. The match is much higher is this area: 64 % of the SfM04 network and 65 % of the LPS-network are identical to the manually digitized network. The main differences occur at the head segments of the drainage network.

The third validation area (VA3) is located in the south-western part. Compared to VA2, the proportion of deeply incised gullies is even higher (75 %) and the amount of shallow gullies is reduced accordingly (23 %). The vegetation-cover is higher compared to VA2, especially near deeply incised gullies. The match between the drainage networks is similar for this area: 67 % for SfM04 and 61 % for the LPS-derived network. However, differences occur mainly at deep gullies, in places where vegetation-cover is patchy.

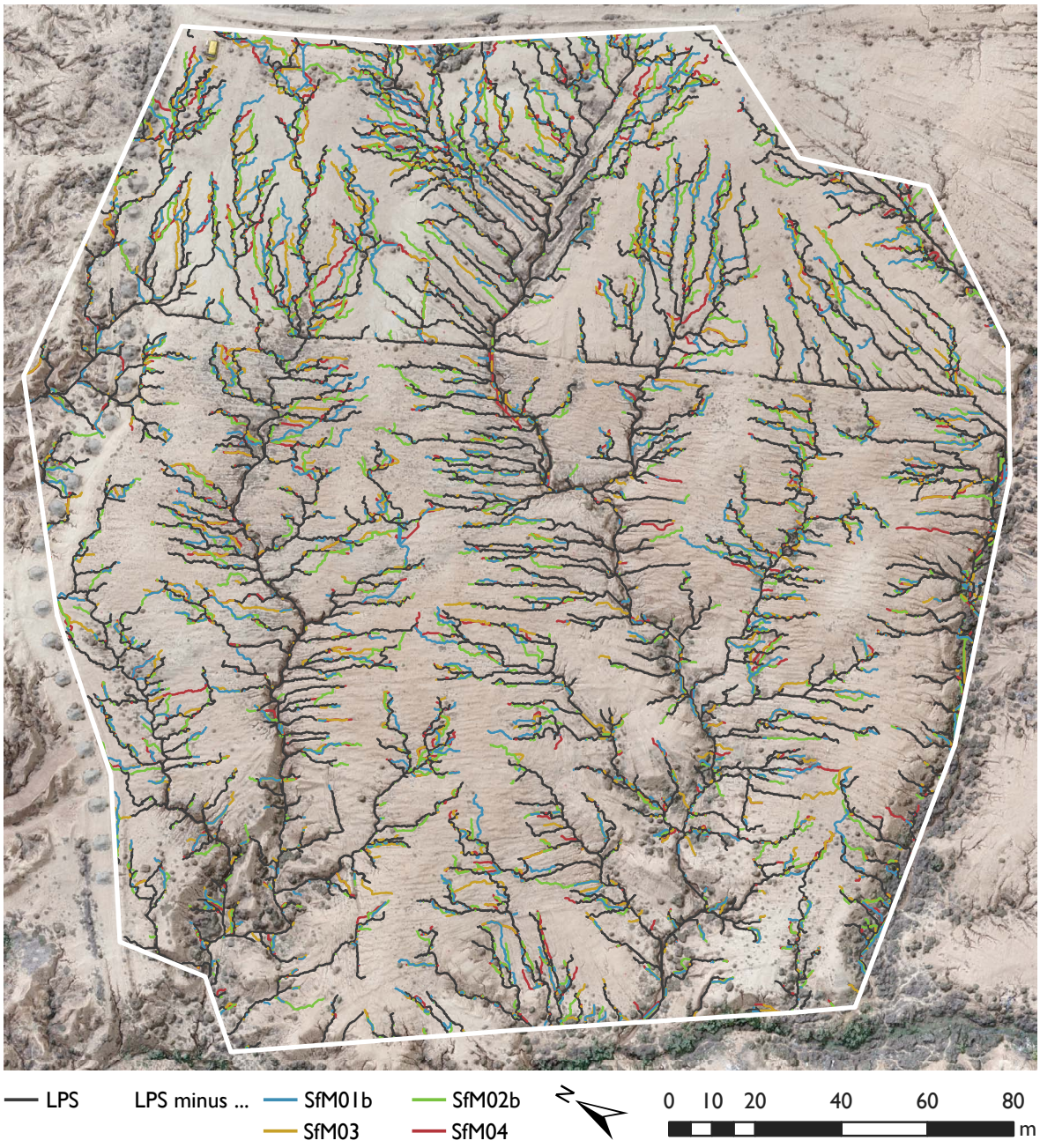

Figure 4.14.: Differences between drainage networks derived from LPS- and SfM-models (the LPS-network is shown completely and the SfM-networks are shown, where they are different to the LPS-network)

Table 4.5.: Quantification of the match between drainage networks derived from LPS- and SfM04-DEMs and validation-network

	validation area 1	**validation area 2**	**validation area 3**
LPS	32 %	65 %	61 %
SfM04	40 %	64 %	67 %

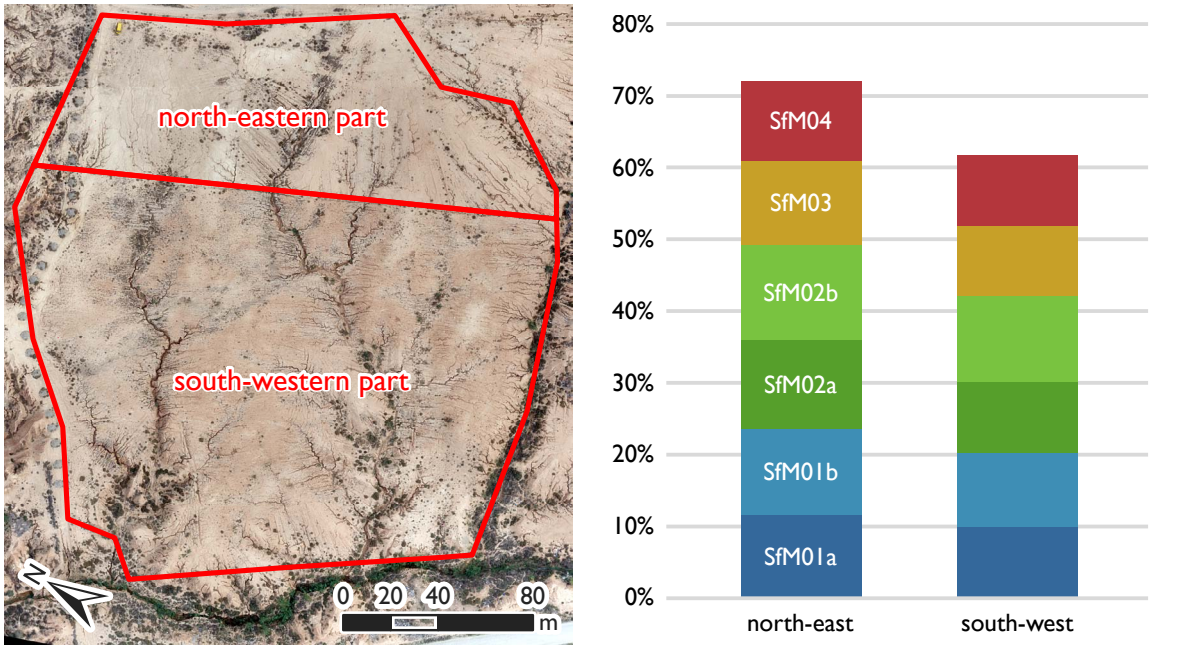

(a) Fragmentation of the area in two sub-areas

(b) Percentage share of total drainage density per SfM-only network

Figure 4.15.: Differences in drainage density per sub-area

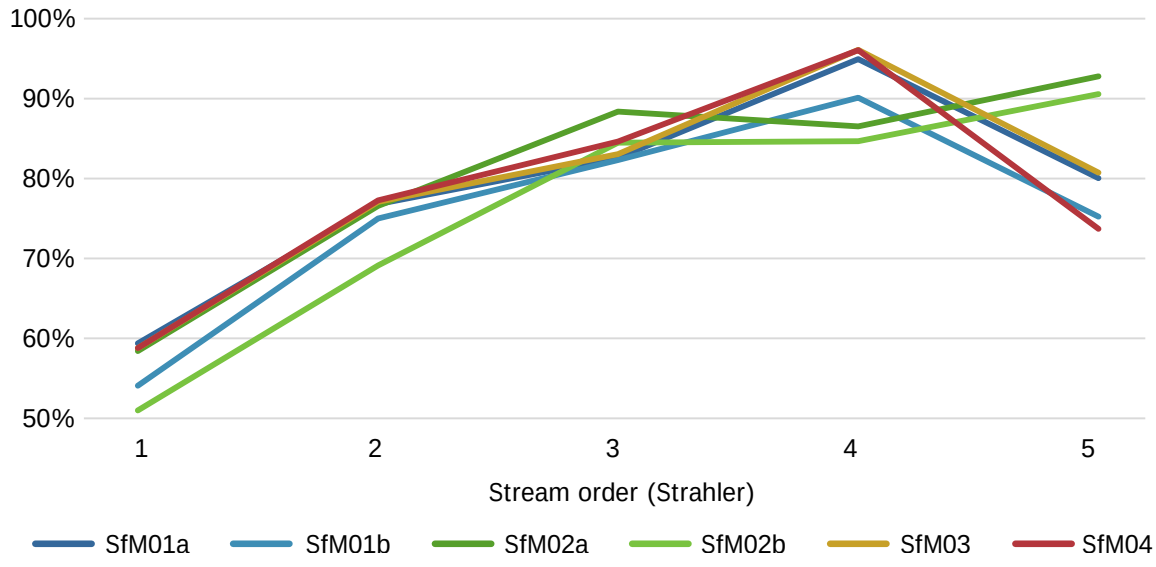

Figure 4.16.: Percentages of the drainage networks derived from the SfM-DEMs that match the LPS-network, differentiated by stream order

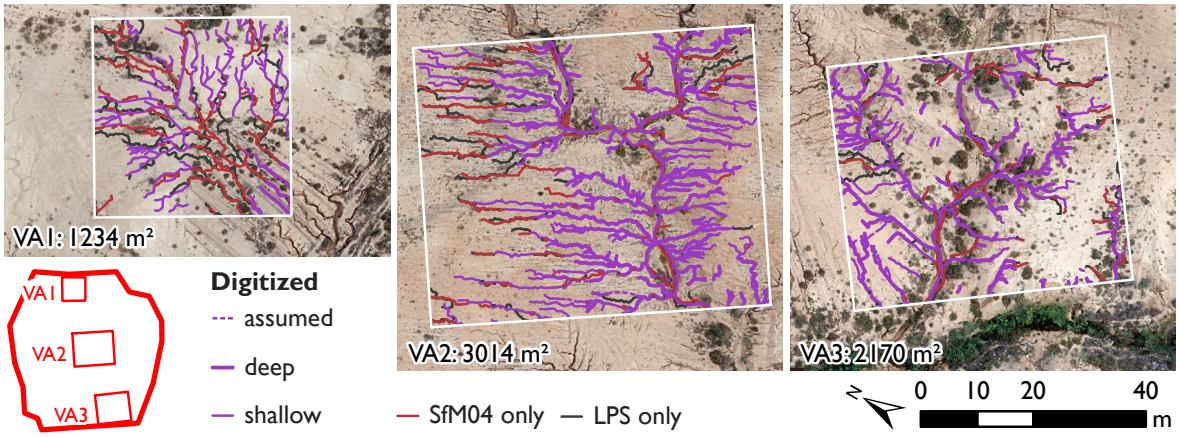

Figure 4.17.: Validation areas (VA1-VA3) with digitized drainage lines and DEM-derived SfM04- and LPS-only drainage lines. Bottom left: location of validation areas within the area of investigation

4.3.3. Watershed Analysis

The results of the watershed analysis are illustrated in Figures 4.19 and 4.20. The differences and similarities between the watersheds are displayed without discriminating between individual sub-watersheds. Green areas indicate those areas of watersheds that were identical for both networks. Red color marks areas that were covered by different watersheds and the colors gray, dark yellow and dark red indicate areas that were only covered by watersheds from one source-DEM. The corresponding percentages are given in Table 4.6, with *first only* and *second only* meaning the first respectively second network mentioned in the headline.

Comparing the watersheds, most areas are identical (71–80 %). This means that these (green) areas drain to the same pour points in both networks. The largest differences can be observed between LPS and SfM04 (Figure 4.19b). Here, 24 % of the area – mainly in the northern part – drain to different pour points for both networks. The discrepancy between LPS and SfM03 respectively SfM03 and SfM04 is smaller (both 17 %), while the amount of congruent areas is higher (77 resp. 80 %). Looking into the detail reveals the reasons for these discrepancies.

Figure 4.18 (left) shows one example for the discrepancy between the watersheds for LPS and SfM04: Due to a slight shift between the networks (approx. 35 cm), the intersection and thus the pour point is located on different segments of the drainage network. Therefore, the watershed for SfM04 was calculated for the drainage line heading west (dark red), while the watershed for the LPS-model was calculated for the drainage line heading north (dark gray). These areas are completely different and one reason for the large differences between the watersheds. This error in particular accounts for 27 % of the differences between LPS and SfM04. Another example is displayed in Figure 4.18 (right). In this case, in the mostly featureless north-eastern part of the area, the dark red watershed overlaying the dark gray area, is much smaller. The reason for this is that the drainage lines for SfM04 (dark red) are separated from those further north-east, while the LPS-network meanders across the area and connects the north-eastern part to the south-western pour point. Drainage lines crossing drainage divides of other networks are the main reason for the differences.

Table 4.6.: Differences and discrepancies between selected watershed-areas derived from LPS-, SfM03- and SfM04-DEMs

	LPS vs. SfM03	LPS vs. SfM04	SfM03 vs. SfM04
discrepancy	17 %	24 %	17 %
congruency	77 %	71 %	80 %
first only	3 %	3 %	2 %
second only	3 %	2 %	1 %

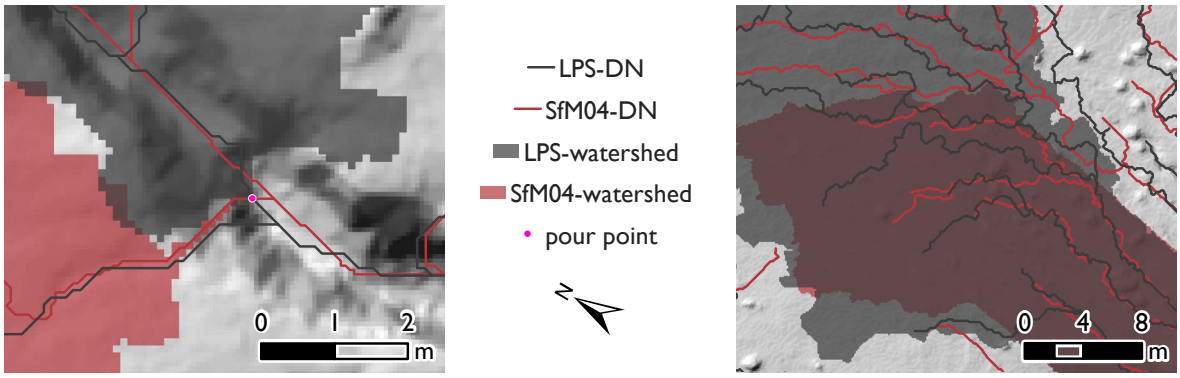

Figure 4.18.: Details of watershed comparison between LPS and SfM04

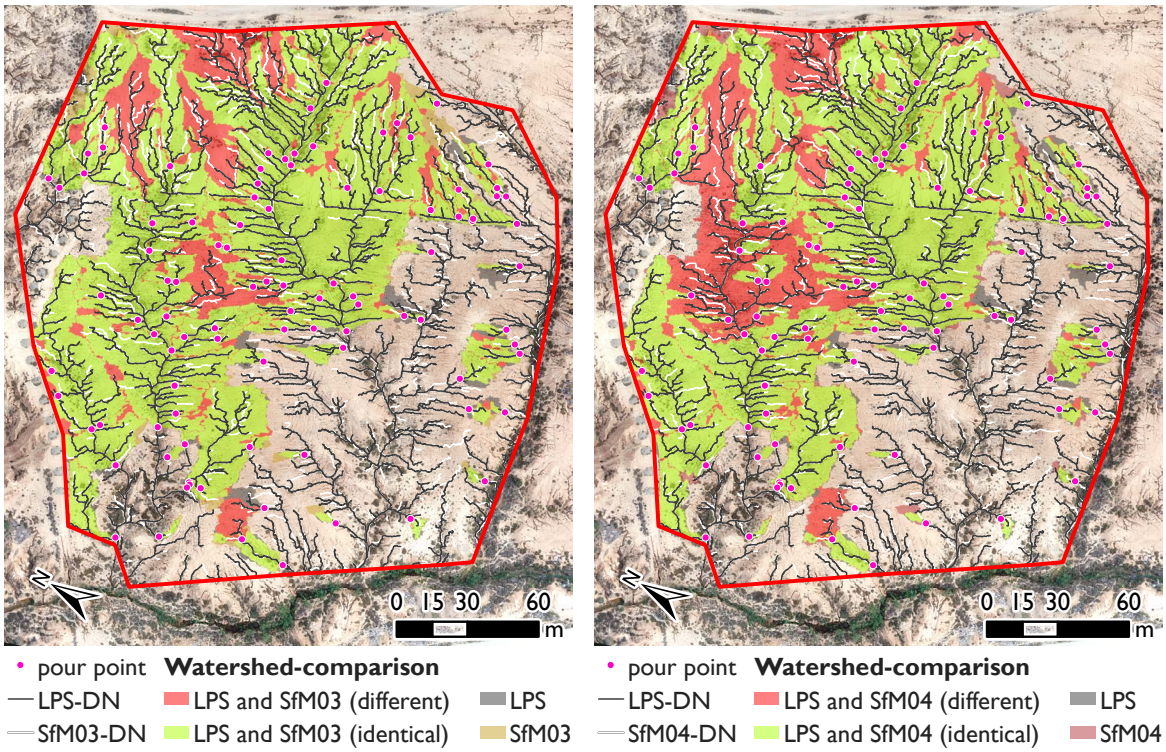

(a) Comparison between selected watersheds, derived from LPS and SfM03

(b) Comparison between selected watersheds, derived from LPS and SfM04

Figure 4.19.: Watershed comparison between LPS and SfM03/SfM04

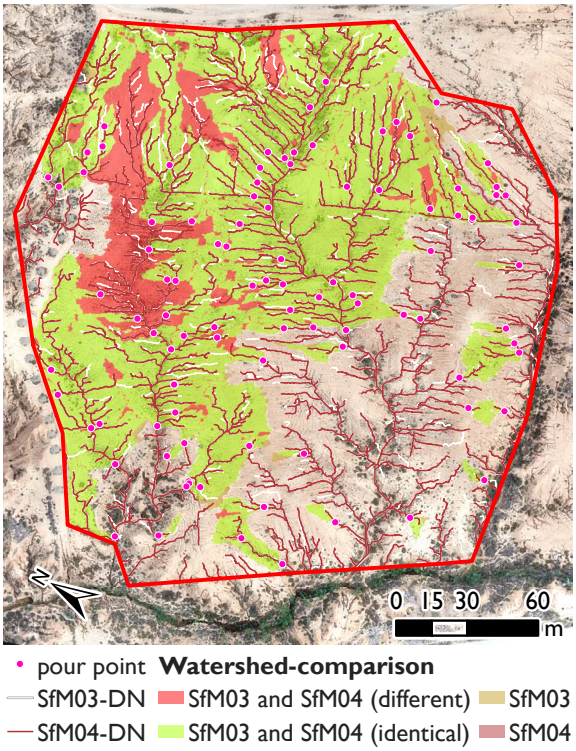

Figure 4.20.: Comparison between selected watersheds, derived from SfM03 and SfM04

5. Discussion

The purpose of this study was to validate the SfM-DEMs from a hydrologic perspective and to evaluate the improvement of hydrologic accuracy when adding more images to the SfM-process. The results described in Chapter 4 are discussed in the following sections and interpreted with respect to other studies.

The first visual impression was that the quality of the DEMs derived using the SfM-approach is much better regarding general noise and artifacts. Nevertheless, this might be due to smoothing algorithms that correct noise and at the same time reduce the amount of details identifiable. This consideration along with the possible influence on hydrologic questions has to be evaluated using quantitative and qualitative analysis.

5.1. Digital Elevation Models in General

The qualitative description of the SfM-DEMs using the shaded relief reveals that the number of images used and the quality – regarding artifacts and noise – seem to correlate. The more images were used, the smoother and less noisy the surface appeared to be. For example SfM02, which uses less images, is slightly worse than SfM01. Although there are less details visible in SfM04 (see Figure 4.1), due to the lower resolution, this model has the least artifacts. The overall impression is that model SfM04 gives the best representation of the surface. Regarding this first visual assessment of the results from the SfM-approach, it may be confirmed that more images lead to higher qualities.

Artifacts are mainly associated with vegetation cover, which is a major problem of the SfM-approach for generating DEMs. This visual impression of the correlation between artifacts (and thus errors) and vegetation was verified in other studies (Westoby et al. 2012: 307; Mancini et al. 2013: 6892; Tonkin et al. 2014: 40; Fonstad et al. 2013: 426), where dense vegetation covers could be related to higher (positive) errors. This behavior is intrinsic for the SfM-approach, since vegetation covers the bare ground and is thus not visible in aerial images. It may only be avoided by filtering vegetation and interpolating the surface for resulting gaps of the point cloud. However, this induces other problems, since vegetation – especially in this area – is mainly present in gullies, where the surface cannot be easily interpolated. Frankl et al. (2015) used SfM to analyze the morphology of gully heads from close distances. They solved the problem of vegetation cover by clearing vegetation prior to data acquisition. They clipped tall grass and larger shrubs that overgrew the gullies (Frankl et al. 2015: 93). However, this may impact the soil surface to be studied and is not easily applicable to larger areas.

The so-called doming effect, as described by James and Robson (2014) and others (see Chapter 2.3), is a major problem in photogrammetric applications. The effect can easily be seen in the visualization

of the DEM-differences between the LPS and the SfM04-DEM (see Figure 4.9). The central part of the LPS-DEM seems to be higher than in the SfM04-DEM. The cause for this error however may not be attributed to the SfM-model. The error values for the GCPs on the LPS-model reveal that the LPS-DEM exhibits – unlike the SfM-DEM – the typical doming effect. All GCPs in the center have a positive Z-error of up to ~10 cm, while the GCPs at the outer margins have large negative Z-errors of up to ~16 cm. The SfM-models do not show this clear trend, although the total Z-errors are not much lower. The difference is that the global fit for both models is similar, but the local fit is better for the SfM-models. The latter means that the doming effect is less significant for these models. This hypothesis can be supported by the distribution of the vertical errors for the GCPs of the LPS- and the SfM01-model (see Figure 4.6). Although the total Z-error of the LPS-model is smaller, the distribution of all vertical errors for the LPS-model is much wider. This confirms once again that the mean error value is not suitable for evaluating the accuracy of DEMs – especially when systematic errors like the doming effect are involved.

Unlike in the study of James and Robson (2014: 1413), who assumed the SfM-approach to be more vulnerable to the problem of the doming effect than the conventional photogrammetric approach – due to less accurate camera models – the SfM-models seem to be more accurate. However, in the present study, the LPS-model exhibits the same problem as the SfM-models, since both methods use a camera self-calibration procedure to compensate for radial lens distortions. James and Robson (2014) proposed to use oblique and convergent images to mitigate the doming effect. They simulated different flight plans involving oblique camera positions and were able to reduce the doming effect by one to two orders of magnitude (James and Robson 2014: 1419). According to them, this would even be possible with the fixed-wing UAV-type used in this study by planning additional, gently curved flight routes above the area. However, using an UAV equipped with a gimbal-mounted camera allows for even more diverse oblique images. As stated before, the images used in this study were not specifically taken to produce SfM-DEMs and the advantages of oblique images were not considered while planning the flights. This is the main reason why the doming effect occurred.

One initial hypothesis was that more images lead to more accurate SfM-models and better representations of hydrologic features. One result that supports this assumption is the correlation between the number of GCP projections and the total GCP-error. The number of GCP-projections is linked to the number of images, since the GCPs are evenly distributed throughout the area. The question, however, is whether the number of images or the number of GCP-projections is crucial for the accuracy. This is because the GCPs are used for the alignment in the SfM-process applied in this study. The reprojection error in contrast is getting larger as soon as more images are used. This is comprehensible, since more images will always introduce more uncertainty to the model. As long as the error is not larger than 1 pix, this should not be a problem. Snavely et al. (2006: 843) tested their newly introduced SfM-system for interactively browsing large collections of photographs with several datasets and calculated an average reprojection error of 1.516 pix. However, they used images from different cameras, viewpoints and from different lightning situation. This increases the difficulty of finding matches between images and may be one reason for the larger error. In another study published two years later, they obtained reprojection errors between 0.418 and 1.36 pix (Snavely et al. 2008: 203).

The smoother surface of the SfM-DEMs may also be explained by statistical values. Regarding the DEM-differences, the standard deviation for the differences between all SfM-models and the LPS-model is highest, presumably because noise in the LPS-model caused the raster of the DEM-differences to vary. This is supported by the standard deviation for differences between SfM-models, which is considerably lower. This implies that the SfM-models are locally more similar. In this context, the mean value is not as meaningful, since it does not reflect local differences. Gatziolis and Fried (2004) analyzed the influence of artificially added *Gaussian* noise on the hydrologic accuracy of derived drainage networks and concluded that this noise slightly improved the accuracy of the perennial stream representation (Gatziolis and Fried 2004: 12). Although they worked on a different level of scale using a 10-m DEM derived from a USGS digital hypsography coverage the results may play an important role in this study: There are large differences between the DEMs regarding the amount of noise.

Using the datasets of the differences between the DEMs as a reference for their similarity, the models of the SfM-variations are more similar compared to each other than the LPS-model compared to the SfM-models. In theory, a mean value close to zero would imply that the DEMs are very similar, while a low standard deviation would suggest that the variance is low and most values are close to this mean value. According to this assumption, the LPS-DEM and SfM01a are very different, compared to the other SfM-variations. However, they all show the previously described doming effect and average values are thus not as meaningful. What can be stated is the general trend that differences between LPS and SfM are larger than between different variations of SfM-models. The more images are involved in the generation of SfM-DEMs, the less differences could be found. This indicates that the result is not random but rather dependent from the methodology and the images used.

Apart from the systematic error across the DEM, the overall magnitude of error is not as bad as expected. Taking into account that images were taken from up to 190 m with a consumer-grade camera and a small UAV, total GCP-errors of approximately 3 cm are small enough for many applications. However, the influence on derived hydrologic data will be analyzed and evaluated in the following sections.

5.2. Drainage Networks

The difference between the total lengths of the drainage networks derived from LPS and SfM01b is highest. This is surprising, since both underlying DEMs were created using the same images and have the same resolution – the only difference was the method used. Furthermore, the drainage network derived from the DEM with the highest resolution (SfM02a) is most similar to the LPS-DN, regarding the total length (-2.6 %). This leads to the impression that there is no correlation between the total length of the drainage network and the resolution of the underlying DEM. However, there seems to be a correlation between the number of segments and the resolution: The lower the resolution, the less segments were detected. This may be explained by the algorithm generating the drainage networks: It is based on pixels and connects them using drainage lines. Using lower resolutions, less details are represented and many small and individual features are merged to single

larger features. However, the influence of this effect is rather small. The amount of segments differs by 4.8 % at most and additionally, these are not necessarily important for the correct representation of the drainage network.

The main reason for the differences in total length is not the amount of segments, but the average length per segment. The average segment has a length between 6.88 m (SfM01b) and 7.68 m (LPS), which is a maximum difference of approx. 11 %. This means that the total lengths mainly differ, because the individual segments are longer. The drainage density varies between 0.2 and 0.23 m^{-1} and behaves identical to the total drainage length – which is consequential, since the reference area is the same. Unlike Goulden et al. (2014: 1918) stated in their study, the drainage densities are not dependent from the resolution of the DEM. This may be due to the lower variation in resolution (between 4.4 and 10 cm), compared to the study of Goulden et al. (2014), where resolutions between 1 and 50 m were analyzed. Within 50 m, it may occur that small drainage lines are summarized, but within a few centimeters, the likelihood of several drainage lines to be summarized is much lower.

To compensate for small, acceptable differences between the drainage networks and in order to consider spatial differences, they were also compared using a buffer. The results indicate that large amounts of the SfM-networks compared to the LPS-model are different (up to 38 %). However, all drainage networks derived from SfM-models have a similar proportion that is only present in their network, compared to LPS. Only SfM01b and SfM02b – the models at a lower resolution of 10 cm – have a larger proportion of drainage lines that are only present in their network. This indicates that the differences between the variations of the DEMs are minor, but there is possibly an influence of resolution. The effect of different resolutions on derived hydrologic features was studied before (see Goulden et al. 2014; Li and Wong 2010; Wu et al. 2008; Wechsler 2007; Hancock 2005; Thieken et al. 1999; Gyasi-Agyei et al. 1995; Zhang and Montgomery 1994). Several parameters that are influenced by the spatial resolution of the DEM were identified: watershed area, stream location and stream length (e.g. Goulden et al. 2014: 1924), slope (Zhang and Montgomery 1994: 1021) and area-slope relationship (Hancock 2005: 1746; Zhang and Montgomery 1994: 1021). However, the differences in resolution in the present study were minor and not necessarily the only reason for systematic differences. This needs to be analyzed in further studies.

The differences in drainage networks were also analyzed with reference to the stream order. The general trend (the higher the stream order, the better the match between SfM and LPS) supports the assumption and visual impression that higher stream orders represent deeper gullies that are equally identified throughout all models. This may be due to better identifiable features and the increased insensibility against small errors.

The vegetation in the present study area has a great influence on the derived drainage networks. Since small bushes and shrubs are mostly represented by small piles in the DEM, the runoff is bypassed which may lead to erroneous networks. However, the correct handling of vegetation is difficult, since both obvious possibilities – leaving the piles as they are and removing them and linearly interpolating the gaps – are not ideal. The true runoff is often far more complex, since vegetation in arid areas often evolves, where small gullies and rigid soil structures provide water and footing for plants. These are often covered by the vegetation and are thus not visible to aerial images and photogrammetric approaches. Even the manual aerial image interpretation to retrieve possible

drainage lines is often not helpful. Tunneling of gullies and shallow drainage lines make it nearly impossible to correctly interpret the images. However for this study, the impact of vegetation may be neglected, because both methods use the same kind of input data and have the same restrictions concerning the vegetation cover.

The match between the drainage networks derived from LPS, SfM04 and the validation networks is slightly higher for the SfM04-network. However, the approach needs to be questioned critically before interpreting the results. The main reason for the differences is the recognition of more drainage lines in the aerial image. There is a clear methodological discrepancy between the two ways of selecting drainage lines. The manual approach of digitizing visual drainage lines disregards the upslope contributing area, while the automatic approach on the other hand uses a consistent threshold for the upslope contributing area to define streams. This highly influences the amount of drainage lines and thus the congruency. In order to get a more consistent approach for both methods, the surface curvature could be used in further studies to identify streams, as proposed by Thommeret et al. (2010).

What can be seen in the validation areas is that the amount of deeply incised gullies is important for the recognition of drainage lines. The larger the proportion of deeply incised gullies, the better the match between the networks. This assumption is supported by the comparison of matches between drainage networks, divided by stream order.

5.3. Watersheds

Finally, the areas of the watersheds were analyzed. According to the data analyzed in the present study, the differences between LPS and SfM04 are highest. The congruency between the watersheds is only 71 %, which means that 29 % of the area analyzed drain to different outlets. However, when looking into detail, the significance of the differences between the models should be revalued. As it could be shown in some cases, small differences in drainage networks, like a shift of 35 cm, can make huge differences. On the one hand, the analysis specifically aimed at finding these issues. On the other hand, small differences will always occur and in this specific case, the method used could be improved.

The first problem was that two different resolutions were compared, which causes the network based on the lower resolution (LPS) to be simplified compared to the other. This results in different drainage lines, no matter how similar the accuracy of both DEMs might be. Secondly, the method of choosing random drainage points might not be ideal, since the observed high discrepancy in watershed area is only existent for a limited area surrounding these points. Some meters further up- and downstream, the watersheds are more similar again. One possibility for evaluating this more realistic would be to weight the differences according to an hydrologic impact factor, which could be based on the upslope contributing area, to diminish errors that are not so important and emphasize those that have a large influence on hydrology. Finally, the amount of data sampled is far too small to draw an explicit conclusion. There is no functional connection between the drainage error and the amount of differences in watershed area. Therefore, it might be hard to find a correlation between the accuracy of DEMs and the congruency of watersheds at all.

The most common cause for different watershed areas are drainage lines that cross drainage divides of other networks due to small differences in the DEMs' elevation and slope. One conclusion that might be drawn for these is that small differences within the DEMs – and conclusively in the derived drainage lines – may cause huge differences in watershed areas and especially in their connectivity.

6. Conclusions

The production of high-resolution DEMs for applications in geosciences and topographic surveying is often outsourced due to high demands in technical and logistic knowledge. These DEMs are often associated with high costs. Within the last decade, *Structure-from-Motion* has become more and more popular for creating high-resolution DEMs, due to a high degree of automation and a great variety of tools that are easy to use. In current studies, this approach, based on well-known photogrammetric principles, was tested for accuracy and often compared to LiDAR- or GPS-data. This work however mainly aimed at validating the SfM-DEMs using derived hydrologic parameters and comparing them to a model created using conventional photogrammetry. The question asked is whether these models are equally suitable for hydrologic applications or not.

The qualitative comparison of the SfM-DEMs and the LPS-model revealed, that the SfM-DEMs can be described as better: The visual impression of the SfM-models is far better compared to the LPS-DEM. There are less artifacts and the surface appears to be smoother and more detailed. Furthermore, the error values of the GCPs for the SfM04-model are smaller and do not show the systematic doming-effect which can be observed in the LPS-DEM. From this general point of view, out of all SfM-models, SfM04 performed best. There seems to be a correlation between the number of images involved in the SfM-process and the accuracy concerning the amount of artifacts and the error values. This confirms the second hypothesis that was made that more images in the SfM-process lead to better DEMs. However, according to several studies, images that are convergent and add new perspectives are more important than redundant images from similar angles. This potential improvement should be considered when further conducting field surveys.

The main question asked in this work was, whether these SfM-DEMs are suitable for hydrologic applications and if there are differences compared to conventional photogrammetry. This cannot be easily answered, since similarities and clear differences could be found: The overall impression of derived drainage networks is good, the main characteristics are the same. However, the derived drainage networks of the SfM-models were up to 9 % shorter in total and had a match of only 62–68 % compared to the LPS-network. Although these values are pretty high, they may not accurately describe the applicability for hydrologic applications, since the hydrologic connectivity may be similar. The main difference occurred in shallow areas, where small differences in height could cause large differences in surface runoff. These differences often caused drainage lines of one network to cross the drainage divide of other networks, resulting in different watershed areas.

This was validated by checking a restricted amount of sample watersheds. The results indicate, that up to 29 % of the watersheds were different, meaning that these areas drained to different pour points. However, the method used does not reflect the whole area of investigation, since the analysis is only valid for the selected points. This procedure could be improved by calculating the upslope

contributing area for each pixel and comparing these values for each pixel and each DEM.

Some problems have been faced during this work. First of all, there is the doming-effect which could not be avoided within this work, since the images already were taken. However, for future field surveys this should be taken into consideration when planning flights. For fixed-wing UAVs, James and Robson (2014) proposed the solution of additional and gently curved flight routes. Multicopters with a camera gimbal offer great advantages and more flexibility, especially in gully-monitoring. They could also be used to take additional close-up images of the gully, adding more detail for these areas. The SfM-approach should be capable of handling these different scales in one calculation.

What remains unanswered in this work is the reason for the artifacts (noise, circles, waves) in the SfM-models. They might be caused by the raw images or the algorithms used within *Agisoft PhotoScan*. Finding a cause for these artifacts would offer the possibility to improve the results. However, as far as *Agisoft PhotoScan* is concerned, the algorithms used are kept secret and are not published to date.

Another issue is the similarity between both methods used to calculate the DEMs. As stated before, conventional and SfM-photogrammetry are developing in similar directions (Fonstad et al. 2013: 422; James and Robson 2014: 1415). In this case, LPS and *Agisoft PhotoScan* both use the GCPs as an input to the calculations, a camera self calibration procedure and a bundle adjustment to calculate the DEMs. Thus, the reference data was not ideal, since similar errors may have occurred in both methods. This could be improved by using a reference data set based on a different technique (e.g. terrestrial or aerial LiDAR).

Another problem was the influence of resolution. Although the differences in resolution for the DEMs used in this work were minor, they may not be neglected. The influence of resolution on hydrologic parameters was already thoroughly tested and confirmed for lower resolutions of several meters and above (Wechsler 2007; Zhang and Montgomery 1994; Wu et al. 2008; Gyasi-Agyei et al. 1995; Goulden et al. 2014; Thieken et al. 1999). It should be verified in further studies if small differences in high resolutions have an influence, too. Additionally, the optimum spatial resolution for hydrologic applications should be re-evaluated. Tarolli (2014: 295) and Hancock (2005: 1745) stated that a spatial resolution of 10 m is adequate for analyzing most hydrologic and geomorphologic processes. However, they also considered the poor availability of (mostly expensive) alternatives. With the decreasing costs of SfM-DEMs this value should be reconsidered.

Finally, the methods applied to determine differences and similarities between hydrologic features could be improved. The buffer method used to calculate the differences between drainage networks does not take into account that drainage lines crossing at right angles are not similar. This was already discussed by Thommeret et al. (2010: 1532), who couldn't find any solution to this problem. This should be improved by adding a functional comparison to the location-based comparison. One possibility would be to somehow introduce the flow direction.

One major result for this work is that the generation of SfM-DEMs is extremely easy and very promising referring to the accuracy in general. Furthermore, the hydrologic applicability and accuracy is very promising but could not be finally determined, due to the systematic problems mentioned before. Further studies of the hydrologic accuracy are necessary, including better reference data and improved methods for comparing hydrologic parameters.

Bibliography

Aber, J. S.; Marzolff, I. and Ries, J. B. (2010): *Small-Format Aerial Photography.* Elsevier, Amsterdam, 1st edition.

Agisoft LLC (2014): Agisoft PhotoScan User Manual: Professional Edition, Version 1.1.

Bartusch, M.; Hajnsek, I.; Janoth, J.; Marschner, C.; Miller, D.; Moreira, P. D. A.; Sparwasser, N. and Zink, D. M. (2009): *TanDEM-X. Die Erde in drei Dimensionen.* Deutsches Zentrum für Luft- und Raumfahrt E.V., Bonn.

Bhiry, N. and Occhietti, S. (2004): Fluvial sedimentation in a semi-arid region: The fan and interfan system of the Middle Souss Valley, Morocco. In: *Proceedings of the Geologists' Association* 115 (4): 313–324.

Bhowmik, A. K.; Metz, M. and Schäfer, R. B. (2015): An automated, objective and open source tool for stream threshold selection and upstream riparian corridor delineation. In: *Environmental Modelling & Software* 63: 240–250.

DeLong, S. B.; Prentice, C. S.; Hilley, G. E. and Ebert, Y. (2012): Multitemporal ALSM change detection, sediment delivery, and process mapping at an active earthflow. In: *Earth Surface Processes and Landforms* 37: 262–272.

D'Oleire-Oltmanns, S.; Marzolff, I.; Peter, K. and Ries, J. (2012): Unmanned Aerial Vehicle (UAV) for Monitoring Soil Erosion in Morocco. In: *Remote Sensing* 4 (12): 3390–3416.

Fonstad, M. A.; Dietrich, J. T.; Courville, B. C.; Jensen, J. L. and Carbonneau, P. E. (2013): Topographic structure from motion: a new development in photogrammetric measurement. In: *Earth Surface Processes and Landforms* 38 (4): 421–430.

Frankl, A.; Stal, C.; Abraha, A.; Nyssen, J.; Rieke-Zapp, D.; De Wulf, A. and Poesen, J. (2015): Detailed recording of gully morphology in 3D through image-based modelling. In: *Catena* 127: 92–101.

Furukawa, Y. and Ponce, J. (2007): Accurate, dense, and robust Multi-View Stereopsis. In: *IEEE Computer Society Conference on Computer Vision and Pattern Recognition*, 1–8. Minneapolis.

Gatziolis, D. and Fried, J. S. (2004): Adding Gaussian noise to inaccurate digital elevation models improves spatial fidelity of derived drainage networks. In: *Water Resources Research* 40 (2): 1–13.

Goulden, T.; Hopkinson, C.; Jamieson, R. and Sterling, S. (2014): Sensitivity of watershed attributes to spatial resolution and interpolation method of LiDAR DEMs in three distinct landscapes. In: *Water Resources Research* 50 (3): 1908–1927.

Grossmann, E. and Santos-Victor, J. (2000): Uncertainty analysis of 3D reconstruction from uncalibrated views. In: *Image and Vision Computing* 18: 685–696.

Gyasi-Agyei, Y.; Willgoose, G. and De Troch, F. P. (1995): Effects of vertical resolution and map scale of digital elevation models on geomorphological parameters used in hydrology. In: *Hydrological Processes* 9: 363–382.

Hancock, G. R. (2005): The use of digital elevation models in the identification and characterization of catchments over different grid scales. In: *Hydrological Processes* 19: 1727–1749.

James, M. R. and Robson, S. (2012): Straightforward reconstruction of 3D surfaces and topography with a camera: Accuracy and geoscience application. In: *Journal of Geophysical Research* 117 (F3): F03,017.

James, M. R. and Robson, S. (2014): Mitigating systematic error in topographic models derived from UAV and ground-based image networks. In: *Earth Surface Processes and Landforms* 39 (10): 1413–1420.

Jenson, S. K. and Domingue, J. O. (1988): Extracting Topographic Structure from Digital Elevation Data for Geographic Information System Analysis. In: *Photogrammetric Engineering And Remote Sensing* 54 (11): 1593–1600.

Jung, K.; Marpu, P. R. and Ouarda, T. B. (2015): Improved classification of drainage networks using junction angles and secondary tributary lengths. In: *Geomorphology* 239: 41–47.

Lehner, B.; Verdin, K. and Jarvis, A. (2006): HydroSHEDS Technical Documentation. Technical report, Washington, D.C.

Li, J. and Wong, D. W. S. (2010): Effects of DEM sources on hydrologic applications. In: *Computers, Environment and Urban Systems* 34 (3): 251–261.

Lillesand, T. M.; Kiefer, R. W. and Chipman, J. W. (2008): *Remote sensing and image interpretation.* John Wiley & Sons, New York, 6th edition.

Lowe, D. G. (2004): Distinctive image features from scale-invariant keypoints. In: *International Journal of Computer Vision* 60 (2): 91–110.

Lucieer, A.; de Jong, S. M. and Turner, D. (2014): Mapping landslide displacements using Structure from Motion (SfM) and image correlation of multi-temporal UAV photography. In: *Progress in Physical Geography* 38 (1): 97–116.

Mancini, F.; Dubbini, M.; Gattelli, M.; Stecchi, F.; Fabbri, S. and Gabbianelli, G. (2013): Using Unmanned Aerial Vehicles (UAV) for High-Resolution Reconstruction of Topography: The Structure from Motion Approach on Coastal Environments. In: *Remote Sensing* 5 (12): 6880–6898.

Marks, D.; Dozier, J. and Frew, J. (1984): Automated Basin Delineation from Digital Elevation Data. In: *Geo-Processing* 2 (3): 299–311.

NASA (2015): U.S. Releases Enhanced Shuttle Land Elevation Data.

Nouwakpo, S. K.; James, M. R.; Weltz, M. a.; Huang, C.-H.; Chagas, I. and Lima, L. (2014): Evaluation of structure from motion for soil microtopography measurement. In: *The Photogrammetric Record* 29 (147): 297–316.

O'Callaghan, J. F. and Mark, D. M. (1984): The extraction of drainage networks from digital elevation data. In: *Computer Vision, Graphics, and Image Processing* 28 (3): 323–344.

Peter, K. D.; D'Oleire-Oltmanns, S.; Ries, J. B.; Marzolff, I. and Ait Hssaine, A. (2014): Soil erosion in gully catchments affected by land-levelling measures in the Souss Basin, Morocco, analysed by rainfall simulation and UAV remote sensing data. In: *Catena* 113: 24–40.

Pike, R.; Evans, I. and Hengl, T. (2009): Geomorphometry: A Brief Guide. In: *Geomorphometry. Concepts, Software, Applications* (Edited by T. Hengl and H. I. Reuter), chapter 1, 3–30. Elsevier B.V., Amsterdam.

Snavely, N.; Seitz, S. M. and Szeliski, R. (2006): Photo tourism: Exploring Photo Collections in 3D. In: *ACM Transactions on Graphics* 25 (3): 835–846.

Snavely, N.; Seitz, S. M. and Szeliski, R. (2008): Modeling the world from Internet photo collections. In: *International Journal of Computer Vision* 80 (12): 189–210.

Tarboton, D. G.; Bras, R. L. and Rodriguez-Iturbe, I. (1991): On the extraction of channel networks from digital elevation data. In: *Hydrological Processes* 5 (1): 81–100.

Tarolli, P. (2014): High-resolution topography for understanding Earth surface processes: Opportunities and challenges. In: *Geomorphology* 216: 295–312.

Tarolli, P. and Dalla Fontana, G. (2009): Hillslope-to-valley transition morphology: New opportunities from high resolution DTMs. In: *Geomorphology* 113 (1-2): 47–56.

Thieken, A. H.; Lücke, A.; Diekkrüger, B. and Richter, O. (1999): Scaling input data by GIS for hydrological modelling. In: *Hydrological Processes* 13: 611–630.

Thommeret, N.; Bailly, J. S. and Puech, C. (2010): Extraction of thalweg networks from DTMs: application to badlands. In: *Hydrology and Earth System Sciences* 14 (8): 1527–1536.

Tonkin, T.; Midgley, N.; Graham, D. and Labadz, J. (2014): The potential of small unmanned aircraft systems and structure-from-motion for topographic surveys: A test of emerging integrated approaches at Cwm Idwal, North Wales. In: *Geomorphology* 226: 35–43.

Triggs, B.; McLauchlan, P. F.; Hartley, R. I. and Fitzgibbon, A. W. (1999): Bundle Adjustment – A Modern Synthesis. In: *Vision Algorithms: Theory and Practice* (Edited by B. Triggs; A. Zisserman and R. Szeliski), volume 1883, 298–372. Springer-Verlag, Berlin, Heidelberg.

Vaze, J.; Teng, J. and Spencer, G. (2010): Impact of DEM accuracy and resolution on topographic indices. In: *Environmental Modelling and Software* 25 (10): 1086–1098.

Vogt, J. V.; Colombo, R. and Bertolo, F. (2003): Deriving drainage networks and catchment boundaries: a new methodology combining digital elevation data and environmental characteristics. In: *Geomorphology* 53 (3-4): 281–298.

Wackrow, R. and Chandler, J. H. (2008): A convergent image configuration for DEM extraction that minimises the systematic effects caused by an inaccurate lens model. In: *The Photogrammetric Record* 23 (121): 6–18.

Wackrow, R. and Chandler, J. H. (2011): Minimising systematic error surfaces in digital elevation models using oblique convergent imagery. In: *The Photogrammetric Record* 26 (133): 16–31.

Wechsler, S. P. (2007): Uncertainties associated with digital elevation models for hydrologic applications: a review. In: *Hydrology and Earth System Sciences* 11 (4): 1481–1500.

Westoby, M.; Brasington, J.; Glasser, N.; Hambrey, M. and Reynolds, J. (2012): Structure-from-Motion photogrammetry: A low-cost, effective tool for geoscience applications. In: *Geomorphology* 179: 300–314.

Wu, S.; Li, J. and Huang, G. H. (2008): A study on DEM-derived primary topographic attributes for hydrologic applications: Sensitivity to elevation data resolution. In: *Applied Geography* 28: 210–223.

Zhang, W. and Montgomery, D. R. (1994): Digital elevation model grid size, landscape representation, and hydrologic simulations. In: *Water Resources Research* 30 (4): 1019–1028.

A. Figures

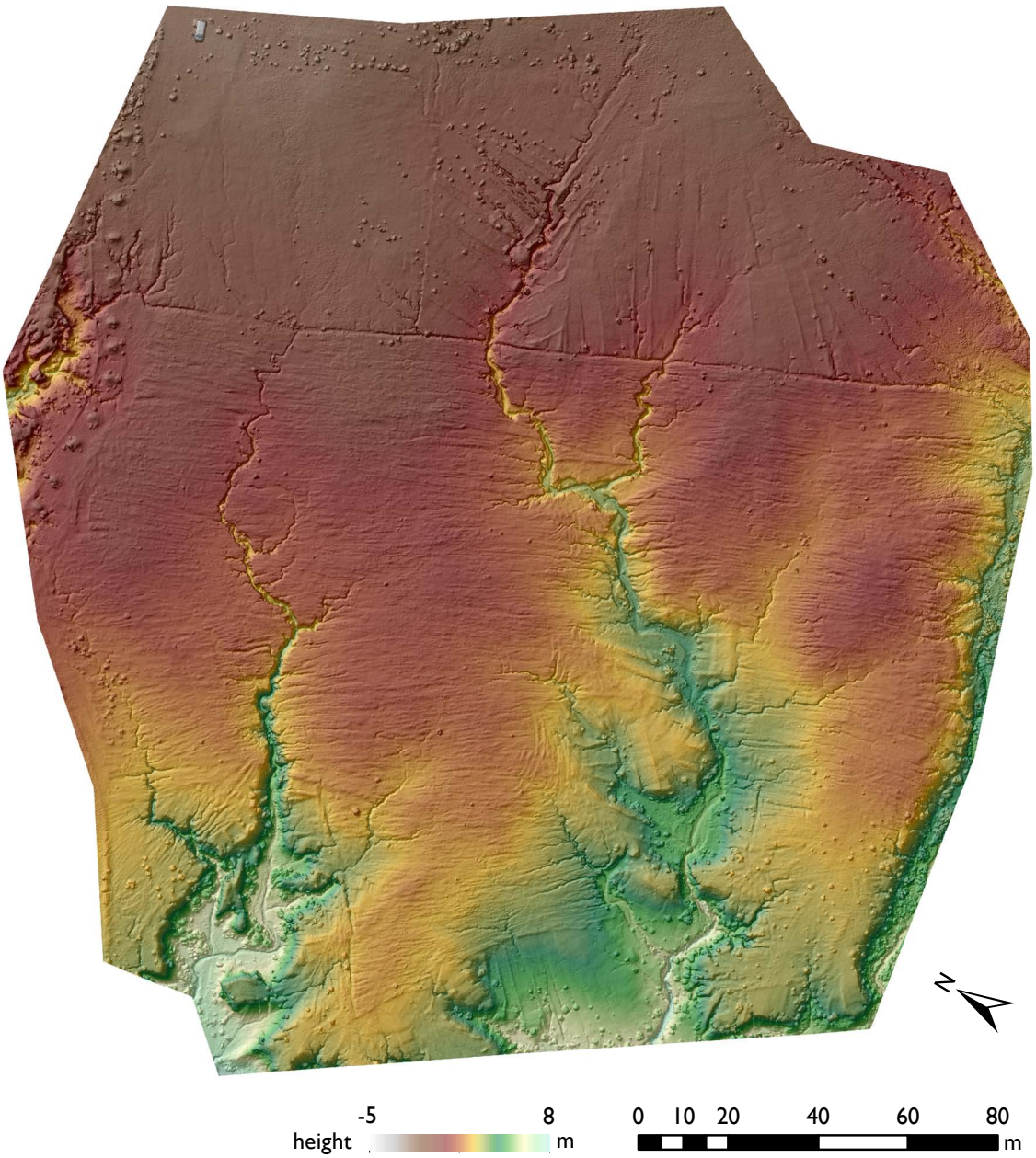

Figure A.1.: Shaded and colored relief of the SfM01a-DEM (4.6 cm)

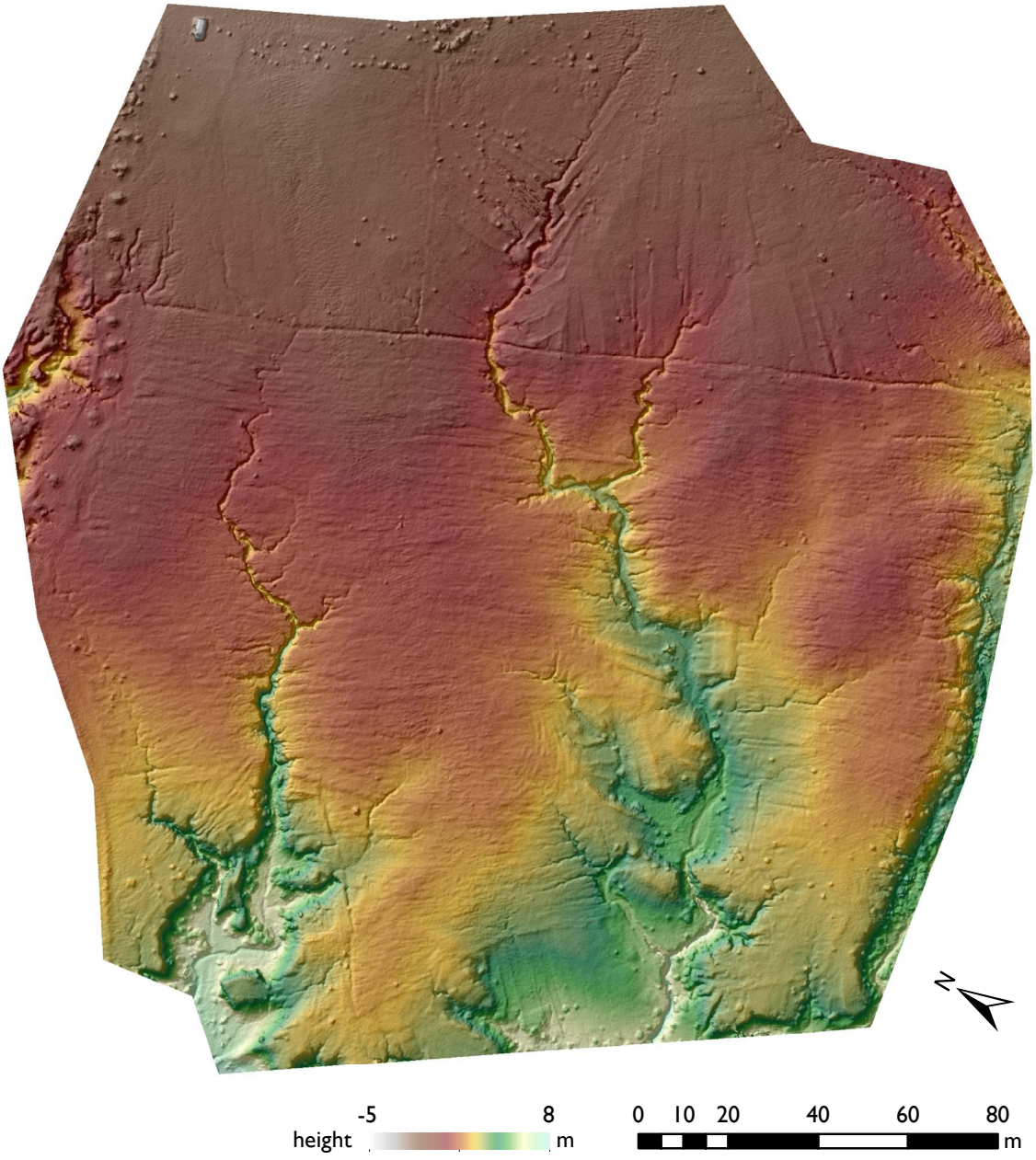

Figure A.2.: Shaded and colored relief of the SfM01b-DEM (10 cm)

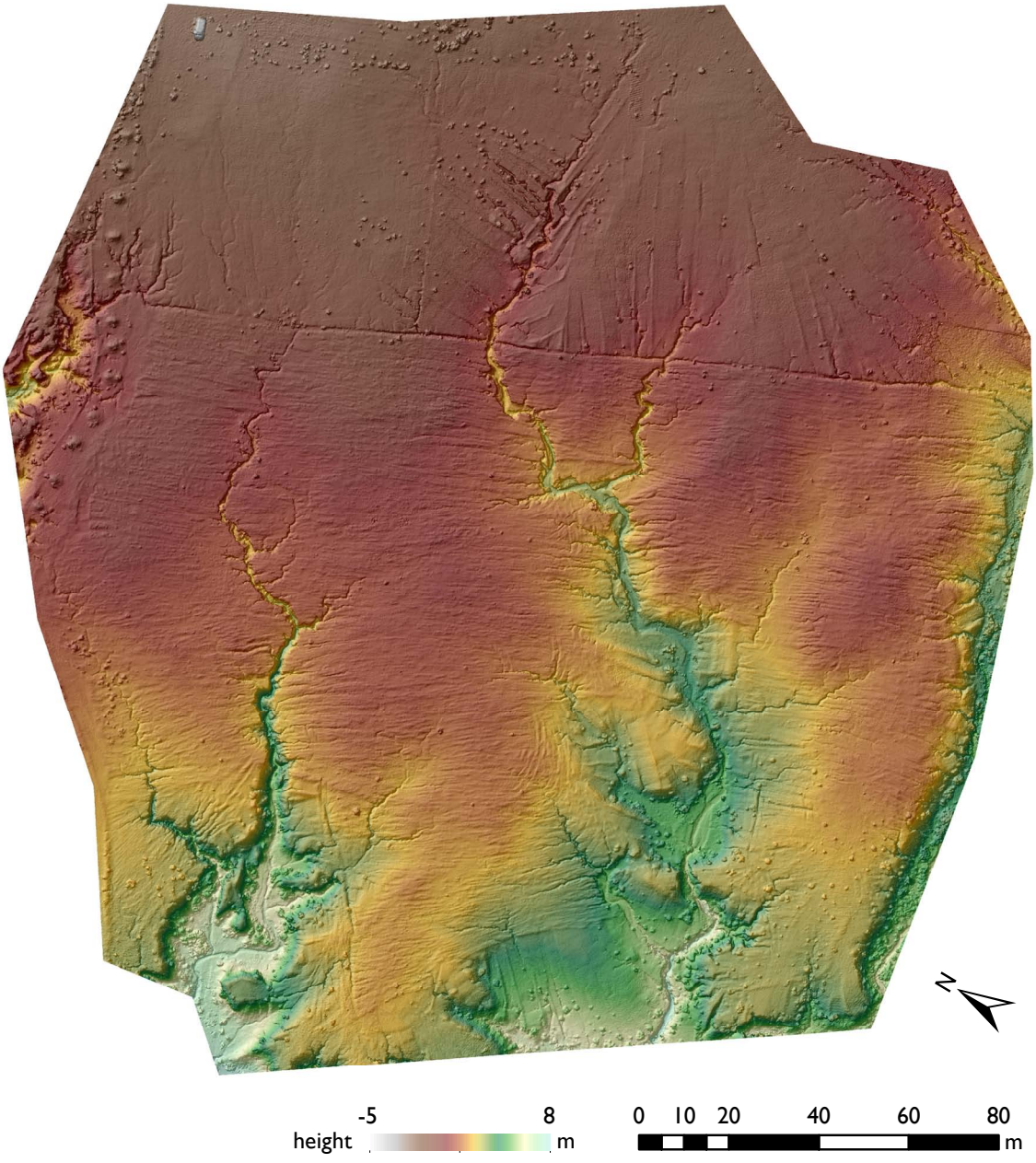

Figure A.3.: Shaded and colored relief of the SfM02a-DEM (4.4 cm)

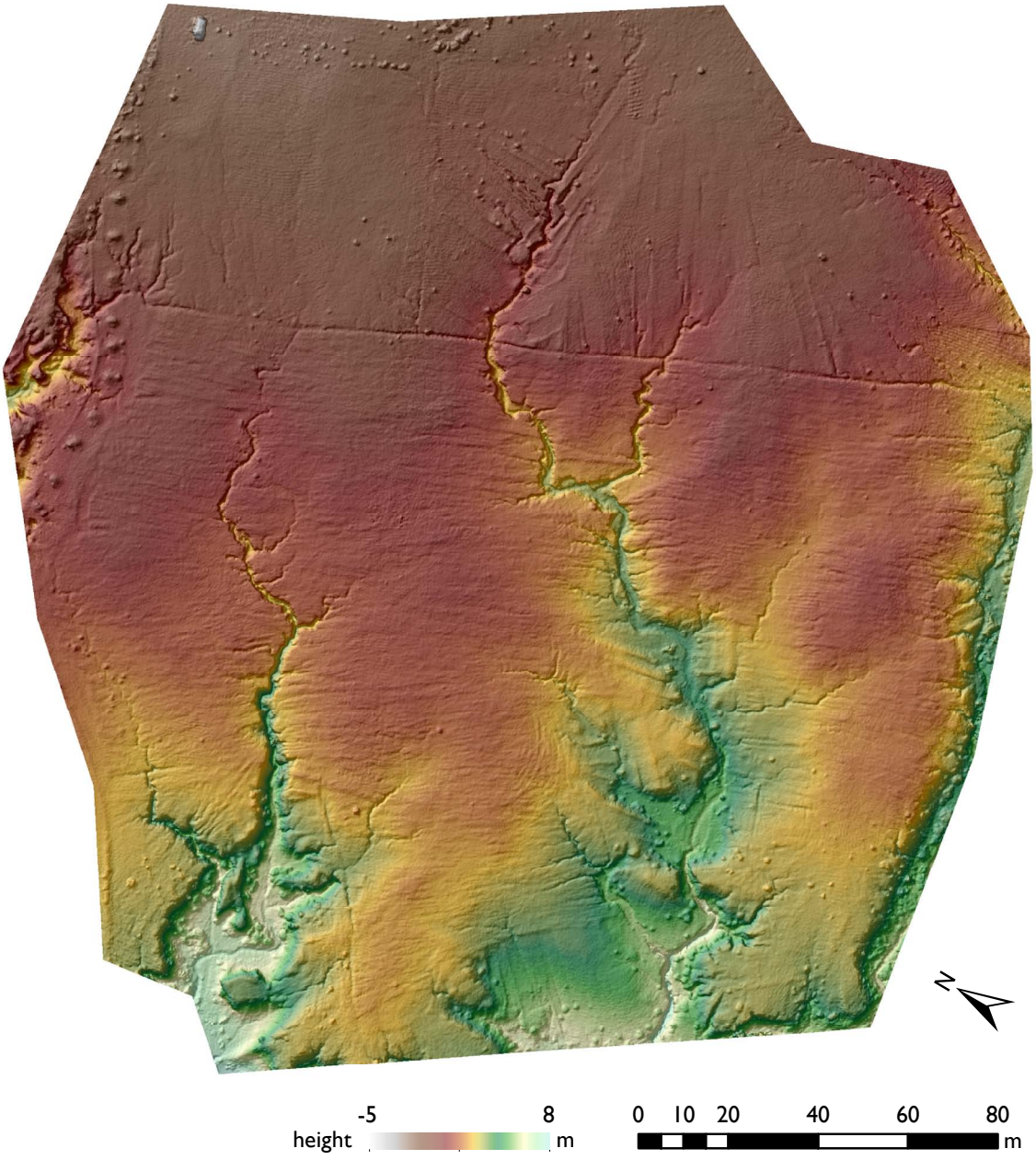

Figure A.4.: Shaded and colored relief of the SfM02b-DEM (10 cm)

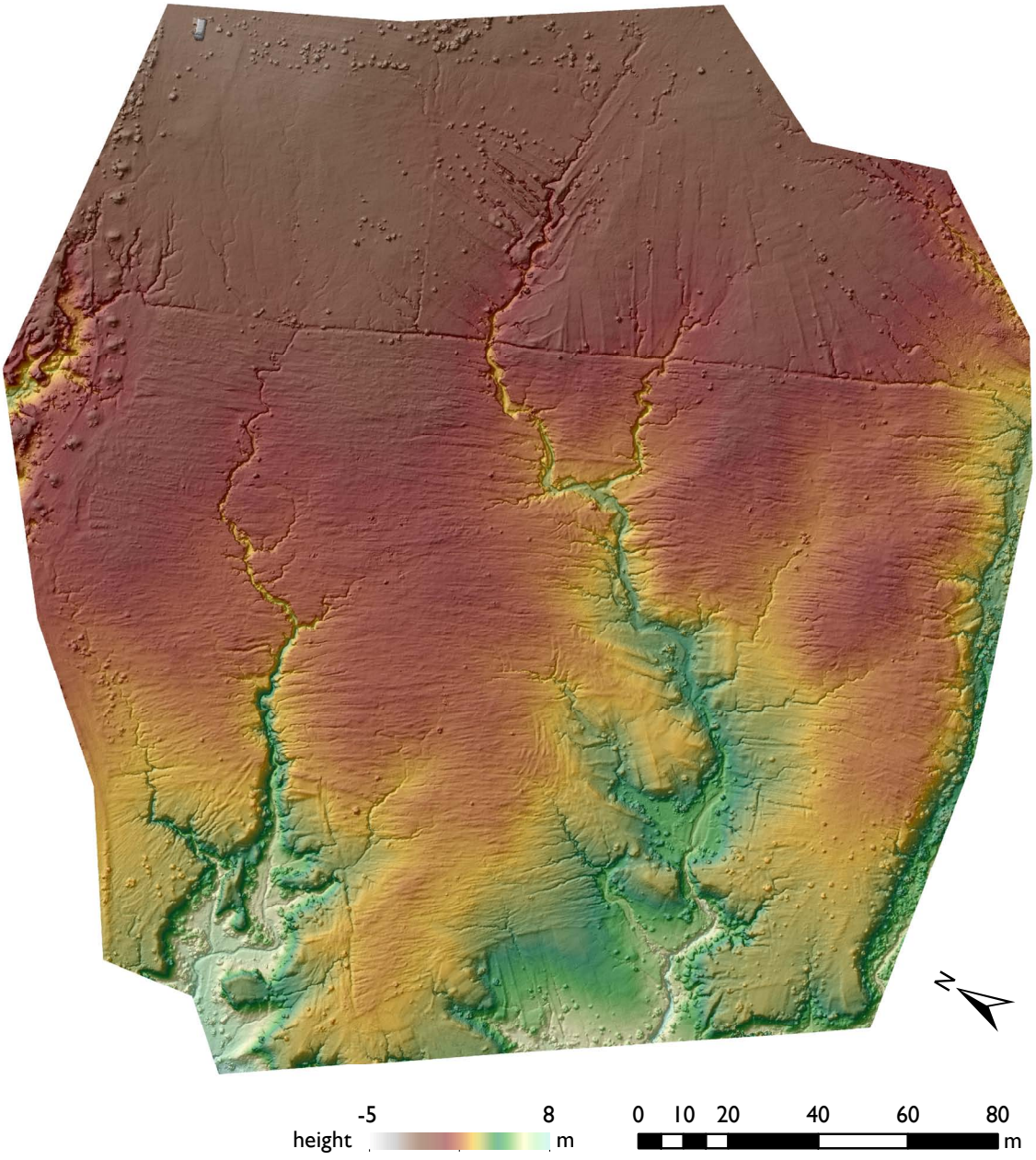

Figure A.5.: Shaded and colored relief of the SfM03-DEM (4.5 cm)

Danke an ...

... Dr. Irene Marzolff und Prof. Dr. Jürgen Wunderlich für die wissenschaftliche Betreuung und Begutachtung der Arbeit sowie ihre Geduld.

... Dr. Irene Marzolff für die Idee und zahlreiche Anregungen zu dieser spannenden Fragestellung.

... Jasmin Fitzpatrick für das Korrekturlesen.

... meine Familie für die Unterstützung während meines gesamten Studiums.

... meinen Freund und Helden Mathias, der immer für mich da war.